Continuous Focusing of Microparticles in Horizontally Actuated Rectangular Channels

Prashant Agrawal,[1,2] Prasanna S. Gandhi,[3] and Adrian Neild[4,*]

[1] *IITB Monash Research Academy, Indian Institute of Technology Bombay, Mumbai, Maharashtra 400076, India*
[2] *Faculty of Engineering and Environment, Smart Materials and Surfaces Laboratory, Northumbria University, Newcastle upon Tyne NE1 8ST, United Kingdom*
[3] *Department of Mechanical Engineering, Suman Mashruwala Advanced Microengineering Laboratory, Indian Institute of Technology Bombay, Mumbai, Maharashtra 400076, India*
[4] *Laboratory for Micro Systems, Mechanical and Aerospace Engineering, Monash University—Clayton campus, Melbourne, Victoria 3800, Australia*

(Received 20 November 2017; revised manuscript received 13 May 2018; published 23 August 2018)

We present a device to continuously focus microparticles in a liquid-filled open channel subjected to lateral vibration at frequencies of the order of 10 Hz. The vibration generates a capillary wave at the liquid-air interface. This capillary wave leads to a net motion of microparticles over multiple cycles, causing collection under the displacement nodes of the capillary wave. These accumulated particles are observed as a concentrated stream in the presence of a continuous flow along the open channel, which means that the channel can be designed such that the focused particle stream exits through one outlet, while the filtrate is removed via interspaced outlets on each side of the particle stream. A numerical model is proposed, which superimposes the periodic flow field due to the capillary wave and the inlet-induced transverse flow field between the inlet and the outlet. The model is utilized to predict the smallest distance from the inlet at which the focused stream of particles is obtained, termed here the collection length. In addition, experiments are performed for different channel and inlet sizes, vibration actuation amplitudes, flow rates, and particle sizes. By considering the design factors extracted from the modeling data, we demonstrate that the resulting device is capable of continuous particle collection down to 1 μm diameter, at flow rates of up to 1.2 ml/min.

DOI: 10.1103/PhysRevApplied.10.024036

I. INTRODUCTION

Various methodologies, over a wide range of system scales, are available for manipulating suspended particles. Macroscale techniques such as centrifugation, sedimentation, and filtration are suited for bulk industrial-scale particle sorting [1], while at smaller system scales, microfluidic platforms enable a relatively high spatial resolution and particle handling dexterity [2]. Such systems either employ complex fluid-structure interactions (passive manipulation [3–6]), or the use of external fields such as dielectrophoresis [7], optical methods [8], magnetic methods [9], and acoustics [10] (active methods), in both batch and continuous modes [11,12]. Passive methods, although simple in operation, provide less control and flexibility due to constrained device design, while active methods, due to the use of an externally controlled field and fluid flow, provide a good alternative for label-free particle manipulation. Comparing the different forcing possibilities, dielectrophoresis and optical methods provide good spatial resolution; however, this advantage comes at a cost in terms of device design and operational complexity. Magnetic fields are restricted to paramagnetic species or require tagging, while acoustic methods provide a low-cost alternative with relatively simple design and operation and operational capabilities over a wide range of particle sizes and system scales (from μm to mm).

When considering acoustic manipulation of particles, it is helpful to define two frequency regimes. At higher frequencies (kHz to MHz), particle manipulation relies on the second-order time-averaged effect of the acoustic fields, which is observed in three different forms: (1) the acoustic radiation force (ARF); (2) the Bjerknes force; and (3) acoustic streaming. The acoustic radiation force is caused by the scattering of acoustic waves on a particle's surface [13], Bjerkenes forces are interparticle forces which are caused by the interaction of a particle with scattered acoustic waves from surrounding particles in the medium [14], and acoustic streaming is a result of time-averaged second-order effects of the acoustic wave on the fluid

*adrian.neild@monash.edu

itself [15,16]. Acoustophoretic particle manipulation can be further divided into two system types, employing either bulk acoustic waves (BAW) [17–21] or surface acoustic waves (SAW) [22–29]. However, regardless of the excitation approach, these systems are designed such that acoustic radiation forces are the dominant particle manipulation forces, causing particles to migrate toward the nodes or antinodes of the pressure wave (depending on the particle's density and compressibility) [30,31]. These forces have been employed in open [32,33] and closed systems to manipulate [17,19,34–41], collect [42], focus [43,44], and sort [26,27,45–48] particles. In addition to the acoustic radiation forces, acoustic streaming is observed as vortices in the liquid bulk (originating due to time-averaged nonlinear terms in the Navier-Stokes equation), which act as drag on the particles, disrupting their migration to stable locations [49–54]. Apart from their applications in mixing [55–58], acoustic streaming has been employed to collect [59–61] and sort [62,63] particulate matter in conjunction with acoustic radiation forces [18,48,64].

However, at lower frequencies (in the 100-Hz range), where particles are susceptible to the first-order periodic fields, particle manipulation is affected through different mechanisms. For instance, particles clump in closed capillary tubes due to boundary-layer streaming on a particle's surface [65,66] and floating particles at a liquid-air interface displace toward nodes or antinodes, depending on their wettability [67], while sediment particles underneath a capillary wave show displacement toward nodes or antinodes [68] due to their inertial lag with the fluid motion [69,70]. In the latter configuration, streaming fields also inhibit stable particle collection [71]; however, by controlling the chamber dimensions and actuation conditions, collection of particles down to 50 nm in diameter has been demonstrated [72,73]. As such, these millimeter-scale capillary-wave systems are capable of collecting submicron-sized particles in batch mode. In contrast, in this work we examine a continuous particle manipulation scheme.

We present a device capable of focusing particles continuously in an open channel by use of low-frequency vibrations. The vibrations generate capillary waves at the liquid-air interface and our experiments show that these waves cause the particles to focus into a single stream even in the presence of an externally imposed flow through the open channel. As well as demonstrating this experimentally, we have modeled the collection using a finite-element simulation. The simulation procedure combines a 3D steady-state transverse flow along the open channel with 2D periodic flows due to capillary-wave vibrations to simulate a particle's path. To allow comparison between simulations and experiments, we characterize performance based on the distance from the inlet to the location at which a focused stream of particles is obtained (termed here the collection length L_c). The result is that despite the simplifications that are required in the model, the simulations agree well with experiments. As a consequence, the simulation model has been used to explain particle-motion characteristics in such open-channel flows, which has assisted in establishing experimental design and operation. The millimeter-scale system presented here is simple in setup and operation, and can achieve particle focusing at flow rates of up to 1.2 ml/min.

II. METHODOLOGY

A. Simulations

The simulation task is to capture the particle motion within an open channel subjected to periodic vibrations and with a net flow along the channel. In such a system, both the particle movement and flow dynamics are nonlinear and occur at multiple time scales. For instance, the periodic vibrations result in a nonlinear particle movement toward the displacement nodes [69], while accompanied by (nonlinear) streaming fields in the liquid bulk, where both aspects relate to the capillary-wave frequency [74]. The net flow along the channel further dictates a time scale, which can be expected to affect the quality of collection at the outlet. Furthermore, the full system is 3D and transient in nature, and has nonlinear components present. As such, a direct simulation approach is prohibitively expensive computationally. Hence, an indirect method is used in which various aspects are captured in different models and the resulting understanding is used to predict the overall behavior. Specifically, the simulation is divided into three separate flow models (Fig. 1): (1) a 3D steady flow field due to the continuous inlet-induced transverse flow; (2) a 2D periodic flow field underneath capillary waves; and (3) a 2D steady streaming field due to the periodically varying capillary-wave field. The overall particle motion is then calculated using a superimposed flow field, allowing the trajectory and the distance from the inlet where the particles attain a stable position in the x direction (the collection length, L_c) to be determined. The inaccuracies resulting from the need to model the capillary-wave fields in two dimensions and the subsequent superposition of the respective fields will be discussed later, in Sec. II A 4.

1. Three-dimensional steady flow

Pressure-driven flows in open channels are accompanied by a varying interface profile along the channel length to compensate for the pressure drop between the inlet and the outlet [75]. The difference between the curvatures at the inlet and the outlet generates the required pressure difference to allow a stable flow, as the Young-Laplace pressure caused by surface tension is curvature dependent. As the channel length, $L = 30$ mm, employed in the present work is significantly larger than the channel width ($W < 10$ mm), the curvature of the interface along

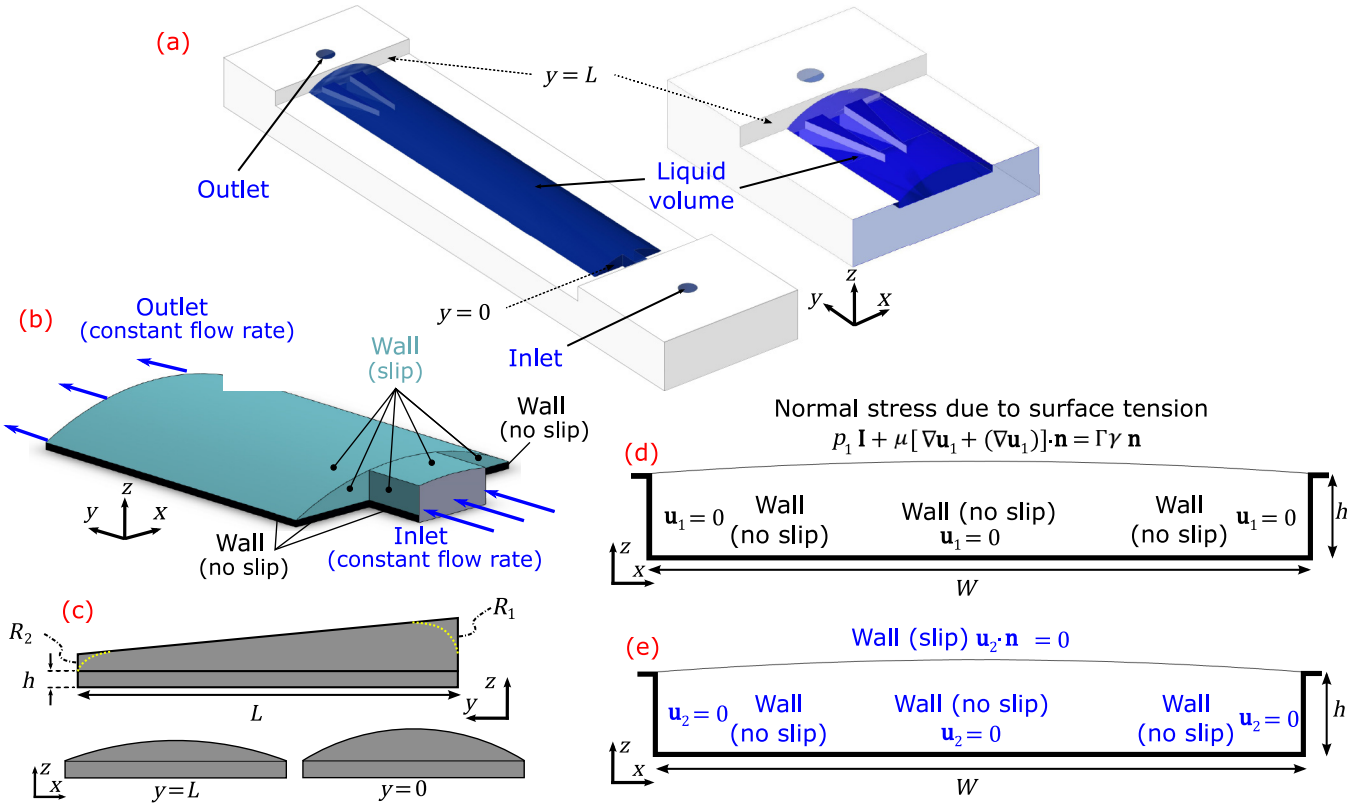

FIG. 1. (a) A depiction of an open-channel geometry for collecting microparticles. (b) The boundary conditions on a liquid volume for modeling the 3D steady inlet-induced transverse flow, detailed in Sec. II A 1. (c) A side view of the liquid volume, depicting the assumed linearly varying interface shape in the y-z plane, R_1 and R_2 are the radii of curvature of the interface in the x-z plane, respectively. The dotted line shows the deformation due to pinning at the ends of the experimental device. (d) The boundary conditions for modeling the 2D periodic first-order flow field in the x-z plane, detailed in Sec. II A 2. (e) The boundary conditions for modeling the 2D streaming field in the x-z plane, detailed in Sec. II A 3.

the channel length [in the y-z plane in Fig. 1(c)] will be smaller than that in the x-z plane. As a result, the pressure at the two ends, with reference to atmospheric pressure, can be given by $p = \gamma/R'$, where R' represents the radius of curvature in the x-z plane at the respective end, and γ is the surface tension at the liquid-air interface; this formulation assumes that the interface profile in the x-z plane is circular, an assumption that is less accurate if $W > L_{\text{cap}}$, where L_{cap} is the capillary length of 2.5 mm. By making this assumption, the pressure difference between the inlet and outlet can be given as follows:

$$\Delta p = \gamma\left(\frac{1}{R_1} - \frac{1}{R_2}\right), \tag{1}$$

where R_1 and R_2 are the radii of curvature across the channel width at the inlet and outlet, respectively. The pressure drop across a channel depends on the flow rate and the channel's length (for a constant channel cross section). Hence, a higher volume flow rate, which requires a higher pressure difference between the two ends, will require a smaller radius of curvature (or a larger liquid height) at the inlet and a larger radius of curvature (or a smaller liquid height) at the outlet.

Neglecting the curvature deformations near the inlet and outlet due to contact-line pinning at planes $y = 0$ and $y = L$, the present model assumes a linearly varying interface shape (along the channel length) between the inlet and the outlet [Fig. 1(c)]. This interface profile is determined for a fixed volume of water contained in the channel. If we assume the interface profile along y and the cross section of the liquid volume in the x-z plane as shown in Fig. 1(c), the volume of liquid in the channel for the model is calculated as follows:

$$V = WLh + \int_{R_1}^{R_2}\left[R^2\sin^{-1}\left(\frac{W}{2R}\right) - \frac{1}{2}W\sqrt{R^2 - \frac{W^2}{4}}\right]dy, \tag{2}$$

where $R = (R_2 - R_1)y/L + R_1$ and W is the width of the channel. Therefore, for a given volume of liquid, multiple sets of inlet and outlet radii of curvature will exist, each set corresponding to a specific pressure difference [Eq. (1)] capable of sustaining a specific flow rate. To find

the curvatures corresponding to the desired flow rate, first, all the sets of possible inlet and outlet radii are identified geometrically from Eq. (2). Next, each obtained geometry is modeled in Comsol, with the boundary conditions depicted in Fig. 1(a), across a range of flow rates, using a 3D steady-state incompressible laminar-flow model. Finally, the pressure difference between the inlet and outlet obtained from simulations is compared with the pressure difference obtained from Eq. (1) to identify the flow rate for the corresponding set of R_1 and R_2. This method is used to avoid the need for a moving-mesh analysis in three dimensions, which is prohibitively expensive computationally. It is important to mention that the above procedure assumes that the liquid-air interface cross section in the x-z plane is circular, which is not true, as $W > L_{\text{cap}}$. However, given the geometrical scale of the system (of the order of 10 mm) and the low scale of Δp (of the order of 0.1 Pa), the exclusion of the effects of gravity on the pressure difference do not correspond to significant variations in the geometry of the liquid volume. Furthermore, additional assumptions in the simulation procedure, detailed in Sec. II A 4, significantly overshadow the effects of the above assumption on the interface curvature.

The obtained 3D steady flow field, denoted by the vector $\mathbf{u}_s$, is later used in conjunction with the 2D periodic flow field.

2. The vibration-induced first-order flow field

The flow field underneath a standing capillary wave comprises of two components: (1) a periodically varying first-order field and (2) a steady second-order field, known as acoustic streaming [72]. The flow field resulting from the horizontal vibrations of the channel is obtained by discretizing the incompressible Navier-Stokes equation using perturbation theory [13], which states that the response of a system perturbed from a state of equilibrium can be represented as a superposition of fields of different orders. Correspondingly, for an incompressible flow, the pressure (p) and velocity fields ($\mathbf{u}$) can be written as follows:

$$\mathbf{u} = \mathbf{u}_0 + \mathbf{u}_1 + \mathbf{u}_2 + \cdots, \tag{3}$$

$$p = p_0 + p_1 + p_2 + \cdots, \tag{4}$$

where the subscripts represent the order of the respective field, p_0 is the reference pressure (atmospheric pressure), and $\mathbf{u}_0 = 0$ considering that the system is initially at rest. At the present operating vibration amplitudes (< 500 μm) and frequencies (< 25 Hz), the capillary-wave amplitude is about two orders lower than the capillary wavelength. In such a case, the magnitude of the transient second-order flow field is significantly smaller than the first-order flow field [76]. Therefore, the transient-flow-field response can be assumed to be dominated by the first-order flow fields.

The first- and second-order flow fields are obtained by inserting Eqs. (3) and (4) into the Navier-Stokes Eqs. (5a) and (5b):

$$\rho_0(\nabla \cdot \mathbf{u}) = 0, \tag{5a}$$

$$\rho_0\left[\frac{\partial \mathbf{u}}{\partial t} + \mathbf{u} \cdot (\nabla \mathbf{u})\right] = -\nabla p + \mu \nabla^2 \mathbf{u} + \mathbf{f}. \tag{5b}$$

Here, μ is the dynamic viscosity of the liquid, ρ_0 is the density of the liquid, and $\mathbf{f}$ represents external body forces acting on the liquid volume. The first-order flow field is found by collecting the first-order terms only:

$$\rho_0(\nabla \cdot \mathbf{u}_1) = 0, \tag{6a}$$

$$\rho_0 \frac{\partial \mathbf{u}_1}{\partial t} = -\nabla p_1 + \mu \nabla^2 \mathbf{u}_1 + \mathbf{f}. \tag{6b}$$

A transient simulation is performed in two dimensions using the boundary conditions shown in Fig. 1(d), applied to a moving-mesh algorithm coupled with an incompressible laminar-flow module. The radius of curvature of the water-air interface is taken to be an average of R_1 and R_2, obtained from the methodology detailed in Sec. II A 1. The contact line is pinned at the top edge of the side walls, which results in a dynamic contact angle as the chamber vibrates. The vibration of the chamber (with amplitude A_0 and angular frequency ω) is implemented as a body force ($\mathbf{f}$) using the following equation:

$$\mathbf{f} = -\rho_0 A_0 \omega^2 \sin(\omega t)\hat{\mathbf{i}} - \rho_0 g \hat{\mathbf{k}}, \tag{7}$$

where g is the acceleration due to gravity. The resonant frequency of the capillary wave along the width (W) in the x-z plane is identified by performing a frequency sweep. While performing a frequency sweep, the velocity magnitude of the flow field (or the capillary-wave displacement amplitude) varies, attaining a maximum at the resonant frequency of the capillary wave. The resonant frequency obtained from this frequency sweep is 12 Hz, which is close to the 12.9 Hz frequency predicted by a 1D capillary-gravity wave model for an infinitely wide fluid volume of depth h, using [76]:

$$\omega^2 = (gk + \gamma k^3/\rho_0)\tanh(kh), \tag{8}$$

where k ($k = 2\pi/\lambda$) is the wave number. Starting from a state of rest, the simulations are allowed to run until the flow field behaves periodically. The x and z components of the flow field (denoted as u_1 and w_1, respectively) are extracted from the last cycle of the simulation, at a resolution of 40 points per cycle. To ease data handling and

reduce computational time, both these variables are fitted as a fifth-degree polynomial, in x and z (using MATLAB's curve-fitting tool), at each temporal point. These approximations for the flow field have been tested with particle movement in 2D systems and have shown to yield particle motion consistent with more direct approaches used previously [69,72].

3. The time-averaged second-order field

The governing equations for the second-order field are obtained by considering the second-order terms, obtained after substituting Eqs. (3) and (4) in Eqs. (5a) and (5b):

$$\nabla \cdot \mathbf{u}_2 = 0, \tag{9a}$$

$$\mu \nabla^2 \mathbf{u}_2 = \nabla p_2 + \rho_0[(\mathbf{u}_1 \cdot \nabla)\mathbf{u}_1 + \mathbf{u}_1(\nabla \cdot \mathbf{u}_1)] + \rho_0 \frac{\partial \mathbf{u}_2}{\partial t}. \tag{9b}$$

Given that the actuation amplitude is approximately two orders smaller than the wavelength of the capillary wave, the magnitude of the second-order velocity field is significantly smaller than the magnitude of the first-order velocity field, at any given time instant [76]. However, the time-averaged effects of this second-order field are observed as steady vortices, termed a streaming field [77], and are governed by the following equations:

$$\nabla \cdot \langle \mathbf{u}_2 \rangle = 0, \tag{10a}$$

$$\mu \nabla^2 \langle \mathbf{u}_2 \rangle = \nabla \langle p_2 \rangle - \mathbf{F}, \tag{10b}$$

where $\langle x \rangle$ represents the time-averaged value of the field variable x. The term $\mathbf{F}$ in Eq. (10b) drives this second-order field and is given by

$$\mathbf{F} = -\rho_0 \langle (\mathbf{u}_1 \cdot \nabla)\mathbf{u}_1 + \mathbf{u}_1(\nabla \cdot \mathbf{u}_1) \rangle. \tag{11}$$

The simulation of the time-averaged second-order fields is a two-step process. First, as a continuation of the vibration-induced first-order field work described in the preceding section, a transient study is conducted over one cycle to establish a value for the term $\mathbf{F}$ in Eq. (11). In this transient study, the first-order flow field Eqs. (6a) and (6b) are solved simultaneously using the following equation:

$$\frac{2\pi}{\omega} \frac{\partial \mathbf{F}'}{\partial t} = -\rho_0[(\mathbf{u}_1 \cdot \nabla)\mathbf{u}_1 + \mathbf{u}_1(\nabla \cdot \mathbf{u}_1)], \tag{12}$$

where the value of $\mathbf{F}'$ at the end of the cycle is equal to $\mathbf{F}$. It is important to mention that the final values of the first-order flow fields obtained from the preceding section are used as the initial conditions in this step. The second step incorporates the obtained value of $\mathbf{F}$ in a stationary laminar-flow model to solve for the steady second-order field $\langle \mathbf{u}_2 \rangle$, using the boundary conditions shown in Fig. 1(e). As with the first-order field, the obtained second-order field is mapped as a fifth-degree polynomial in x and z.

4. Flow-field integration

Assuming linear flow conditions, the 2D and 3D fields obtained from the previously discussed models are superimposed to obtain the final flow field:

$$u = u_s + u_1, \quad v = v_s, \quad w = w_s + w_1. \tag{13}$$

Here, the velocity field with subscript s is the 3D steady inlet-induced flow field (Sec. II A 1) and the velocity field with subscript 1 indicates the 2D first-order periodic flow field (Sec. II A 2). Particle motion is traced by importing the superimposed velocity-field data into MATLAB and cycling it to replicate the effect of a periodic field.

The above methodology has been developed as it enables a way of arriving at a flow-field result without incurring prohibitive computational requirements. It considers a decoupled field resulting from the capillary-wave vibrations and from the inlet-induced transverse flow. To achieve this, it has been necessary to make several assumptions, which cause the following factors to be neglected:

1. The interface curvature along the channel length (in the y-z plane). The interface curvature along the channel length is assumed to be zero [Fig. 1(c)]. Although this is partially true for a large part of the channel along y (considering that $L \gg L_{\text{cap}}$), there will be a significant curvature at the inlet and outlet due to contact-line pinning at the respective channel boundaries [depicted by dashed lines in Fig. 1(c)]. This curvature will alter the inlet-induced transverse flow and the capillary-wave-induced periodic flow fields significantly.
2. Variable interface curvature (in the x-z plane) along the channel length. As mentioned in Sec. II A 1, the radius of curvature of the interface in the x-z plane is higher at the outlet (R_2) compared to the inlet (R_1), as depicted in Fig. 1(c), thereby leading to an increasing radius of curvature along the channel length from the inlet. Although the present model assumes a linear variation of radius of curvature for the simulation of the inlet-induced transverse flow field, the modeling of the 2D periodic flow field assumes a constant radius of curvature throughout. A varying radius of curvature will not only change the u_1 and w_1 fields at each cross section, but will also give rise to a periodically varying y component of the first-order flow field (v_1).
3. The no-slip boundary condition at the inlet or outlet for the $\mathbf{u}_1$ field. A no-slip boundary condition exists at the inlet (plane $y = 0$) and outlet (plane $y = L$), due to

contact-line pinning; therefore, a boundary layer will exist near these planes. As a result of this boundary layer, the capillary-wave velocity field magnitude will increase from the aforementioned planes; the boundary-layer thickness is of the order of 0.1 mm and is estimated by $\delta = \sqrt{2\mu/\omega\rho_0}$ [76]. However, as mentioned earlier, the $\mathbf{u}_1$ field is taken to be constant all throughout the channel length, thereby neglecting the above no-slip condition.

4. The effect of the periodically changing interface shape on the inlet-induced transverse flow. The model for the inlet-induced transverse flow field in Sec. II A 1 considers the interface shape to remain constant at all times. However, the periodic vibrations alter the interface shape and, therefore, will also contribute to a periodically varying inlet-induced transverse flow field.

5. The streaming field. Streaming fields originate due to the presence of spatial velocity gradients in a time-periodic field [77]. All of the above-mentioned flow characteristics of the present system will generate spatial gradients in the flow, thereby contributing to a 3D streaming field, the effects of which cannot be predicted accurately using the 2D modeling procedure described in Sec. II A 3. Neglecting the presence of a streaming field imposes a significant constraint on the modeling procedure, as they not only affect the collection speed of particles (which affects the collection length), but also determine the conditions in which particles get collected stably [72].

The above assumptions are incorporated in our model due to the high computational requirements of modeling 3D first- and second-order flow fields. Although these assumptions limit the accuracy of this model, we find that the model is able to provide a reasonable estimate of the collection length of the particles in the channel and of the trends with regard to how this measure changes over a range of other parameters.

5. The particle-tracing algorithm

The particle's motion in the superimposed flow field $\mathbf{u}$ is traced using the equation $m_p\ddot{\mathbf{x}} = \mathbf{F}_p$, where m_p is the mass of the particle, $\mathbf{x}$ is the position vector of the particle, and $\mathbf{F}_p = \mathbf{F}_v + \mathbf{F}_S + \mathbf{F}_{\mathrm{VM}}$ is the force acting on the particle, comprising of the following forces [78]:

(1) Viscous drag forces (given by the Khan and Richardson expression for the particle Reynold's number [1] $\mathrm{Re}_p = \rho_0|\mathbf{u} - \mathbf{u}_p|2r/\mu > 0.01$):

$$\mathbf{F}_v = \pi r^2\rho_0|\mathbf{u} - \mathbf{u}_p|(\mathbf{u} - \mathbf{u}_p) \times [1.84\mathrm{Re}_p^{-0.31} + 0.293\mathrm{Re}_p^{0.06}]^{3.45}. \quad (14a)$$

(2) The force due to pressure stresses on the particle surface:

$$\mathbf{F}_S = \rho_0 V\dot{\mathbf{u}} - (\rho_p - \rho_0)Vg\hat{\mathbf{k}}. \quad (14b)$$

(3) The virtual mass force ($\mathbf{F}_{\mathrm{VM}}$):

$$\mathbf{F}_{\mathrm{VM}} = \frac{\rho_0 V}{2}(\dot{\mathbf{u}} - \dot{\mathbf{u}}_p). \quad (14c)$$

Here, r is the particle's radius, ρ_p is the particle's density, V is the volume of the particle, and $\mathbf{u}_P$ is the particle's velocity vector. The particles are spread all across the width and height of the inlet at $y = 0$ at the start of the simulation. The force F_p is assumed to be acting at the center of the particle, while the finite size of the particle is assumed to have no effect on the flow field. Further, the presence of hydrodynamic interactions from the wall and the presence of rotational lift forces [79] acting on the particle are neglected.

B. Experiments

1. Device fabrication

The open channels are fabricated using polydimethylsiloxane (PDMS) cast in a mold with features of thickness (h) 200 μm to form the shape and size channels; an example of a channel design used in the present experiments is shown in Fig. 2(a). All channels have a length (L) of 30 mm and two different widths (W) of channels are used: 8 and 5 mm. These widths correspond to one capillary wavelength at frequencies of 13 and 22 Hz, respectively. Such low operating frequencies ensure that streaming fields are not dominant, while the collection forces are strong enough to ensure a focused particle stream well before the outlet is reached [74]. For the channel with $W = 8$ mm, the inlet width (W_i) is varied from 1 to 8 mm. The mold is fixed to the base of a container and PDMS (Sylgard; elastomer: curing agent weight ratio = 10 : 1) is poured over the mold and allowed to cure at 75°C until solidification. Two separate PDMS blocks are fabricated, as shown in Fig. 2(b), and these act as an inlet into and an outlet out of the channel. These inlet and outlet blocks are joined with the channel using PDMS, while ensuring that the ports are not blocked during assembly. Proper alignment also ensures that the central outlet port is equidistant from the two side outlets, ensuring equal flow rates from each of these outlets. The assembly is then allowed to cure on a hot plate (at 75°C) until the blocks are firmly joined together. The design shown in Fig. 2(b) is used for characterization only, while the design shown in Fig. 2(e) is employed to separate the filtrate and the concentrated particle stream.

2. Setup and operation

The experimental setup is shown in Fig. 2(d). The device is mounted on an electromagnetic shaker (Brüel and Kjaer,

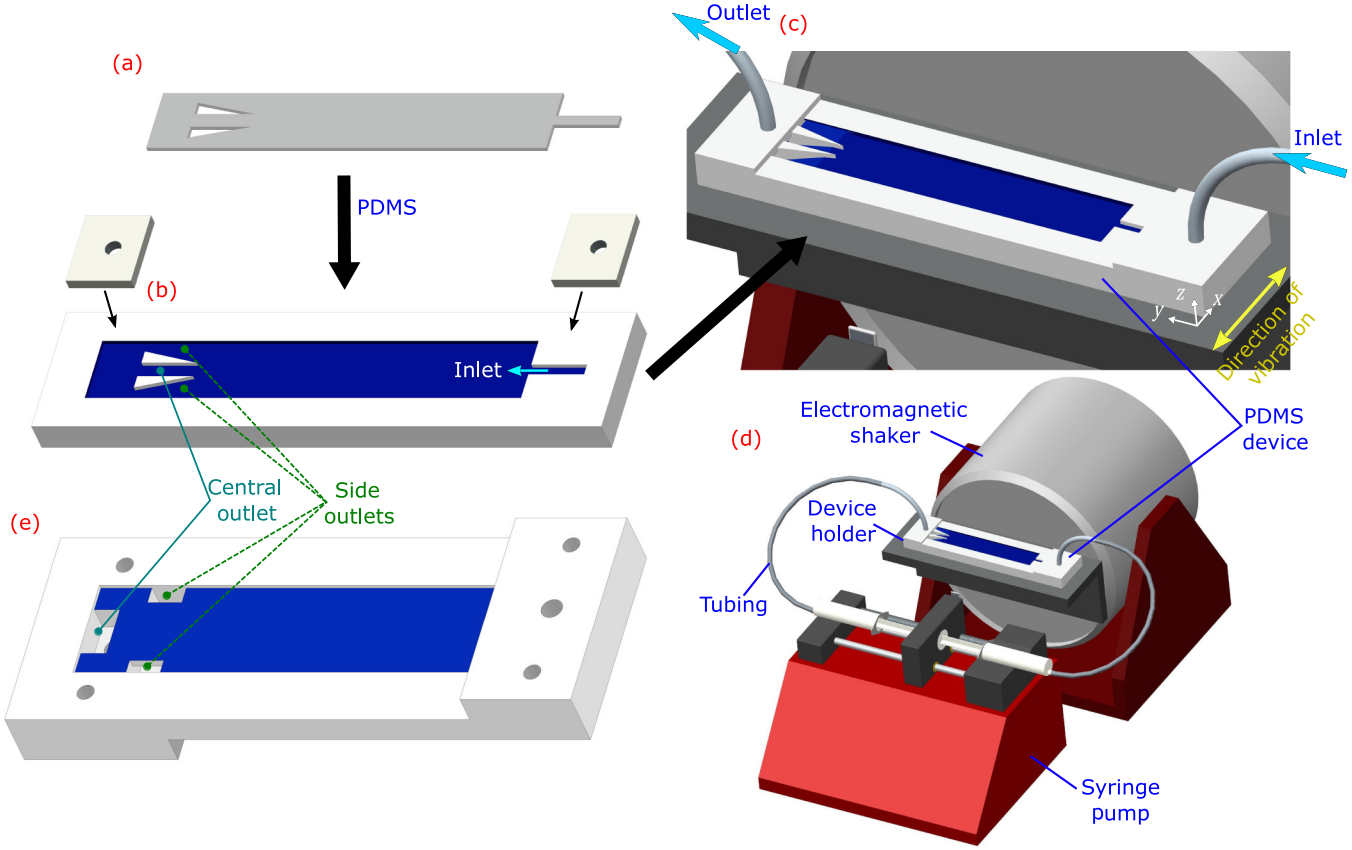

FIG. 2. (a) The mold for creating a PDMS open channel. (b) The PDMS channel obtained after curing. (c) The final open channel with attached inlet and outlet blocks. (d) A schematic of the experimental setup. (e) An alternate channel design used for separating the filtrate and the particle concentrate.

LDS V406/8) and the channel's inlet and outlet ports are connected to a syringe pump (NE-1000, New Era Pump Systems), which simultaneously infuses and extracts particle suspensions at equal flow rates within the range from 0.3 to 1.2 ml/min. The shaker, which provides the required lateral actuation, is driven by a signal generator (Agilent 33220A) via a power amplifier (Brüel and Kjaer, PA 200E) and the actuation amplitude is measured using a laser-Doppler vibrometer (Polytec MSA-500). Silica particles of 5 μm diameter and polystyrene particles of 1 μm diameter are used in the experiments. Before starting the flow, the channel is prefilled with water. This ensures that the inlet and outlet ports are connected by the liquid volume and remain so throughout the experiment run time (about 12–15 min). In the absence of this prewetting procedure, the liquid forms a bulge at the inlet which grows radially, rather than advancing along the channel length, eventually spilling over the sides of the open sunken channel, while the outlet takes in air [75]. Further, the volume of water used for prefilling allows other factors to be accounted for, as follows.

First, there exists a critical volume of liquid below which the volume demonstrates properties similar to those on a homogeneous surface and is prone to a capillary breakup along the channel length [80]. Above this critical volume, the liquid volume remains stable and is bounded by the walls of the channel. The high-contact-angle hysteresis obtained at the top edge of the perpendicular (or obtuse) solid surface also assists in containing the liquid volume [81,82], allowing the liquid to bulge out of (but not spill out of) the channel area. However, the contact-angle hysteresis is overcome on increasing the liquid volume further and spillage occurs. In the present case of a vibrating liquid-air interface, it should be additionally considered that the prefill volume is limited to ensure that spilling does not occur (or the contact line remains pinned to the channel edges) for the desired vibration amplitudes.

Second, as mentioned in Sec. II A 1, a flow along the channel will alter the radii of curvature (in the x-z plane) along the channel length, based on the flow rate. A higher flow rate requires a higher pressure difference between the inlet and the outlet, which will correspond to a smaller radius of curvature (or a greater liquid height) at the inlet, and a larger radius of curvature (or a lesser liquid height) at the outlet. As the flow rate increases, the height of the fluid at the outlet drops, which determines a critical flow rate

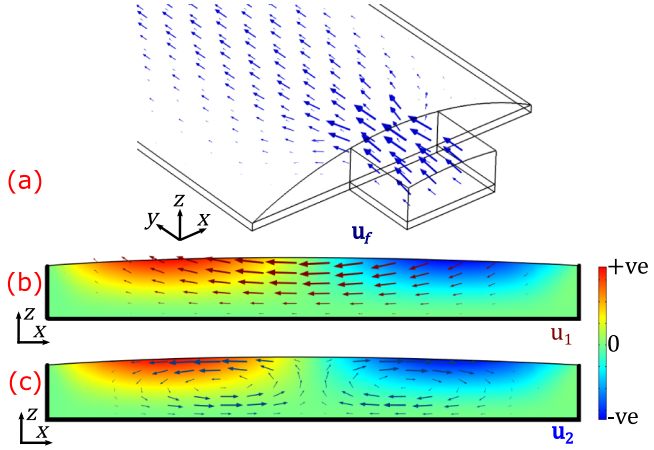

FIG. 3. (a) The 3D steady inlet-induced transverse flow field. (b) The 2D (first-order) periodic flow field at time $t = 0$: the surface plot depicts the w_1 field. (c) The 2D (second-order) streaming field: the surface plot depicts the w_1 field.

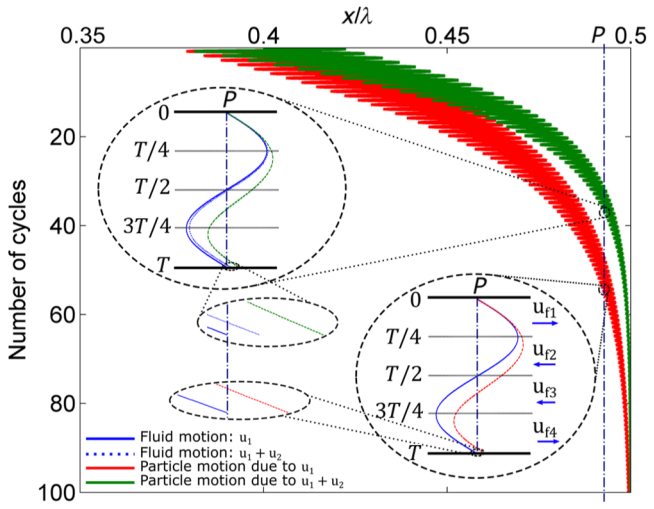

FIG. 4. The difference in particle motion under the influence of the $\mathbf{u}_1$ (red) and $\mathbf{u}_1 + \mathbf{u}_2$ (green) flow fields. u_{f1}, u_{f2}, u_{f3}, and u_{f4} represent the average u_1 flow-field strengths in the depicted time intervals over a cycle. The flow-field strength decreases from $x = P$ to $x = 0.5\lambda$.

limit for a consistent and stable flow, for a given channel length and a given inlet and outlet geometry [75].

Considering these factors, for a channel of dimensions $30 \times 8 \times 0.2\ \text{mm}^3$, a prefill volume of 200 μl is found suitable for operation up to a vibration amplitude of 500 μm and a flow rate of 1200 μl/min. After the experiment run time of about 12–15 min, the filtrate is scanned using dynamic light scattering (DLS; Malvern Zetasizer Nano ZS) to detect the presence of any particles.

III. RESULTS AND DISCUSSION

In the following sections, we examine a particle's response to the simulated flow fields and determine the distance from the inlet at which a focused stream of particles is obtained. As we employ a simplified equivalent model for simulating a particle's motion in a complex 3D flow field, the limitations and errors associated with such a model, while comparing with experiments, will also be highlighted.

A. Simulations

The three flow fields, the vibration-induced periodic first-order field, the vibration-induced steady second-order field, and the steady inlet-induced transverse flow field, are shown in Fig. 3. Particle motion under the influence of the vibration-induced first- and second-order fields has been explored extensively in a 2D-cross-section chamber in our previous works [72,74]. Here, we first briefly describe particle motion under the influence of these 2D fields, while later including the inlet-induced transverse flow to characterize the particle's motion along the channel in Sec. III A 2.

1. Particle motion due to the capillary-wave vibrations

We will consider particle collection under a capillary wave which is one wavelength long. This choice both simplifies the collection and/or concentration procedure experimentally and is favorable with regard to the effects of streaming [72], as will be discussed later in this section. The movement of a solid particle (red) in a periodically varying flow field $[u_f(x,z)\cos(\omega t)]$ of one wavelength is shown in Fig. 4. Due to its finite inertia, the solid particle's motion deviates from that of a fluid particle. As a result, the particle experiences different flow fields at different instances in the cycle [69] on either side of the fluid particle's motion. If the motion of the particle over a cycle is split into four quarters, as shown in the inset in Fig. 4, the average flow-field strength that the particle experiences at different instances in the cycle can be assessed based on its relative position with the fluid particle. Consequently, the following inequalities can be written:

$$u_{f_1} > u_{f_2} > u_{f_3} \approx u_{f_4}. \tag{15}$$

As the movement of a particle is dictated by the drag encountered by it, the particle's direction of displacement can be estimated by the following expression [72]:

$$\Delta x_P \propto (u_{f_1} - u_{f_2} - u_{f_3} + u_{f_4}), \tag{16}$$

which, in the context of the inequalities in Eq. (15), corresponds to the displacement of a particle toward $x = \lambda/2$, i.e., toward the region of slower fluid flow; Δx_P is the displacement of a particle at P.

Parameters affecting collection.—The parameters affecting the speed of collection due to the first-order flow field are as follows:

1. Vibration amplitude (A_0). A higher amplitude is, unsurprisingly, reflected in the magnification of the flow-field magnitudes; therefore, Δx_P increases directly from expression (16), resulting in a faster collection. The collection forces, denoted as F_{eq}, vary as approximately A_0^2 with the actuation amplitude [70].
2. Channel width (W). A smaller channel width is accompanied by an increase in the operating frequency [from Eq. (8)]. Due to the reduction in the distance needed for reaching the collection location, as well as the increase in collection force as a result of increasing frequency [74], the collection speed increases with decreasing channel width ($F_{\text{eq}} \propto W^{-3.5}$).
3. Chamber height (h). The chamber height has a very minimal influence on the collection speed [70] ($F_{\text{eq}} \propto h^{0.1}$).
4. Particle radius and density (r, ρ_p). The particle displacement depends on the phase difference (ϕ) between the movement of the solid and the fluid particle, which depends on the particle density and radius; these are qualitatively related as [1,69] $\tan\phi = -2\rho_p r^2\omega/9\mu$. For the present operating frequency range (10–30 Hz), an increase in the particle inertia increases the phase difference ϕ and thus increases the collection forces [70]. While an increase in both r and ρ_p increases the collection forces, the simulations show that the particle radius has a significantly higher effect on the collection force ($F_{\text{eq}} \propto r^2$) compared to the particle density ($F_{\text{eq}} \propto \rho_p^{0.02}$) [70].

The parameters discussed above also affect the streaming fields. In the next section, we examine the constraints that the streaming field imposes on the channel design.

Effect of streaming field.—The presence of streaming does not alter the direction of motion of the particles while being collected [as shown in Figs. 3(c) and 4]. However, it does affect two important factors: (1) it affects the speed with which the particles collect and (2) it introduces a second outcome for the particles; other than collecting, the streaming can cause particles below a critical size to swirl in the streaming flows [72]. As the u_2 streaming field converges toward the collection location (underneath the capillary-wave node), the net displacement of the particle over a cycle is significantly enhanced. However, as the particle approaches the collection location, the w_2 streaming-field strength increases [Fig. 3(c)]: this vertical flow causes drag forces which oppose the gravitational pull on the particle. As such, there is an increased tendency for the particle to dislodge from the base and circulate in the streaming flows, thereby inhibiting stable collection (which, in the absence of streaming, would be under the capillary-wave node). This tendency for liftoff is, therefore, dictated by a balance between the upward drag due to the streaming field ($6\pi\mu r w_2$) and the downward-acting buoyancy-corrected weight [$4\pi(\rho_p - \rho_w)r^3 g/3$].

Hence, for a given flow field (driven by a given actuation amplitude and frequency, and present in a channel of specific width and depth), a set of particle radii and density values exists, above which the particles collect into stable locations, while below this set of values, the w_2 field dominates and lifts the particles into the swirling patterns present in the liquid bulk. This set of values, termed the cutoff values, is highly critical in determining the appropriate set of actuation conditions for collecting a given set of particles [74]. As per Eq. (11), the streaming-field strength depends on the flow-field magnitude and gradients, which depend on the actuation amplitude and vibration frequency; an increase in either increases the streaming-field magnitude. As a result, although an increased streaming-field magnitude can increase the speed of collection, it also increases the cutoff values of the system [74], which implies that more particle types will not be collected.

In the next section, we add the effect of the inlet-induced transverse flow field on the particle's motion to determine the distance from the inlet at which the particles converge to form a focused stream.

2. Particle movement along the channel: 3D motion

The trajectory of particles (in the x-y plane), obtained from simulations, as they enter the collection channel from the inlet is depicted in Fig. 5. As a particle enters the collection channel, it is subjected to drag forces from the inlet-induced transverse flow field as well as from the vibration-induced flow field.

For the channel geometry shown in Fig. 2, where the widths of the inlet and the collection channel are different, the particle experiences a drag force F_{dx} from the inlet-induced transverse flow as it enters the collection channel. The magnitude of F_{dx} depends on the channel geometry and the flow rate. When this force is stronger than the collection force F_{eq} (from the periodic field), the particle diverges from the center, while traversing in the y direction [as depicted in Fig. 5(a)]. Further downstream, as the inlet-induced transverse flow direction aligns with the channel length, F_{dx} reduces, causing the particles to move toward the center of the channel due to the dominant F_{eq}. Thereafter, the particles continue as a focused stream and exit through the central outlet of the channel. The distance from the inlet at which the width of the particle stream becomes 10% of the inlet width is defined, here, as the collection length, L_c. Based on the depiction of forces in Fig. 5(a), L_c can be expressed in terms of the respective forces by the following expression:

$$\frac{W_i}{2L_c} \propto \frac{F_{\text{eq}} - cF_{dx}}{F_{dy}}, \tag{17}$$

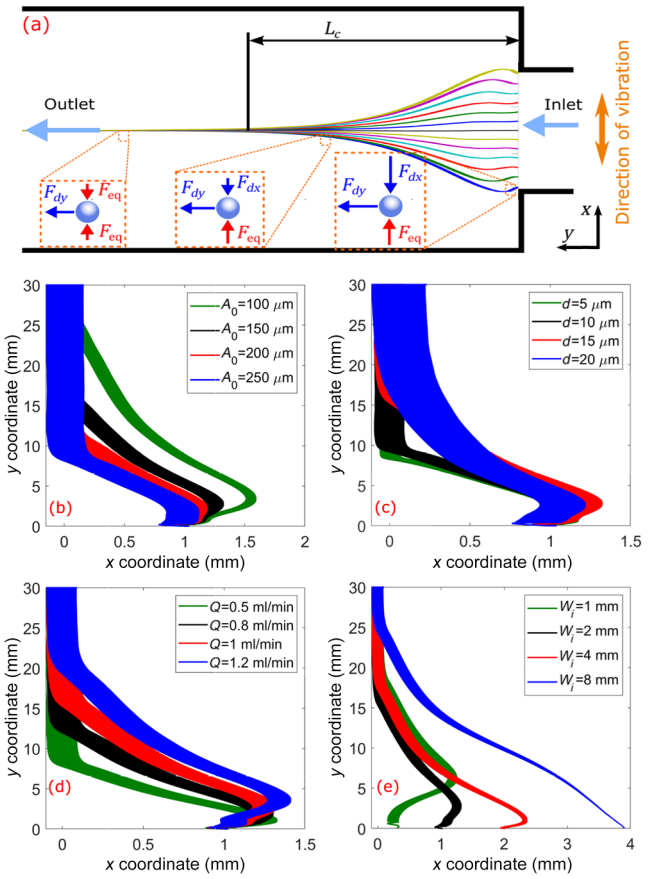

FIG. 5. (a) A depiction of the movement of particles and the relative forces acting on them along the channel from the inlet to the outlet. (b)–(e) Particle trajectories ($\rho_p = 2000$ kg/m^3) in the x-y plane for varying: (b) vibration amplitude ($W_i = 2$ mm, $Q = 1$ ml/min, $d = 15$ μm); (c) particle diameter ($W_i = 2$ mm, $Q = 1$ ml/min, $A_0 = 150$ μm); (d) volumetric flow rate ($W_i = 2$ mm, $A_0 = 150$ μm, $d = 15$ μm); and (e) inlet width ($Q = 1$ ml/min, $A_0 = 150$ μm, $d = 15$ μm). Q is the volumetric flow rate, W_i is the channel inlet width, A_0 is the actuation amplitude, and d is the particle diameter.

where c signifies the contribution of F_{dx} on the particle's x movement compared to the equivalent collection force F_{eq}. The factor c primarily depends on the ratio between the inlet width and the channel width.

Parameters affecting collection.—As seen from Eq. (17), an increase in F_{eq} decreases the collection length L_c. Therefore, as discussed in Sec. III A 1, for an increase in A_0, a decrease in W (or an increase in f), and for particles with higher r and ρ_p, the collection forces will increase; thereby, the collection length will decrease. A similar observation can be made for the effect of drag forces due to the inlet-induced transverse flow field (F_{dx} and F_{dy}) on L_c. For instance, an increase in the flow rate Q will increase both F_{dx} and F_{dy}, resulting in an increase in L_c. With regard to the inlet width W_i, for a constant flow rate, a decrease in W_i will increase the flow velocity in the area near the inlet, thereby increasing F_{dx} and F_{dy}, which leads to a decrease in the right-hand side of Eq. (17). However, the left-hand side also decreases due to W_i, which leaves an interplay of two effects which can affect the variation of L_c. As a result, the simulations show that with increasing inlet width, the collection length first decreases and then, at higher values, starts to increase, as shown in Fig. 5(e).

TABLE I. The range of parameters considered in the simulations for characterizing the collection length L_c.

Parameter	Range	Base value
A_0 (μm)	100–500	200
Q (ml/min)	0.3–1.2	1
W_i (mm)	1–8	2
$d = 2r$ (μm)	5–20	15

Simulations are performed by varying different parameters to determine the collection length. L_c is determined at the distance in y from the inlet where the width of the particle stream becomes 5% of the inlet width. Each parameter is varied as per the range mentioned in Table I, while the other parameters are kept constant at the listed "Base value." The following best-fit empirical correlation is obtained with $R^2 > 0.95$ for all the data sets obtained from the parametric simulations:

$$\frac{W_i}{2L_c} = 0.08\frac{A_n^{0.1}}{Q_n^{0.9}}(2.9 + 11.7r_n - 134.9r_n^2) - 0.15\frac{A_n^{0.2}}{Q_n^{0.8}}\left(1 - \frac{W_i}{W}\right)^2(2.1 + 17.4r_n - 137.4r_n^2), \tag{18}$$

where $A_n = A_0/\lambda$, $Q_n = Q/(A_0\omega Wh)$, and $r_n = \beta r$; $\beta = \sqrt{\omega/2\nu}$ and ν is the kinematic viscosity. We note that the effect of the channel length L on L_c is not discussed here. The channel length is determined by the flow rate constraint, as mentioned in Sec. II A 1. Although, due to the change in interface profile, the channel length will affect both the first- and second-order flow fields, we do not undertake the variation of channel length in this study because its corresponding 3D streaming effects cannot be modeled with the present technique, as mentioned in Sec. II A 4.

Effect of streaming field.—We must also consider the effect of streaming in the 3D system. Although the 2D model used provides a good estimate of the cutoff characteristics for a batch collection system [72], the same model cannot be employed to fully capture the 3D characteristics of streaming. The presence of a significant v_2 field alters the cutoff characteristics of the system [73] as well as the collection length. Furthermore, it becomes essential to

TABLE II. The variation of L_c with Q in hypothetical flow fields of varying strengths of the streaming field in the y direction (v_2). The table lists the value of the exponent b in $L_c \propto Q^b$ for varying magnitudes of the v_2 field. Here, $s = 1$ implies that the magnitude of the assumed v_2 is the same as that of the u_2 field modeled as detailed in Sec. II A 3.

W_i (mm)	$s = 0$	$s = 0.1$	$s = 0.5$	$s = 1$	$s = 2$
1	1.22	1.21	1.19	1.18	1.15
2	0.98	0.82	0.78	0.74	0.66
4	0.94	0.73	0.66	0.58	0.47
8	0.91	0.72	0.65	0.58	0.47

consider the first-order flow field in the y direction (v_1), in regard to particle-movement and streaming-field calculations, as the nature of the system will result in significant spatial gradients in the v_1 field (based on the discussion in Sec. II A 4). These gradients affect the u_2 and w_2 field while giving rise to vortices in the x-z plane (similar to a vertically actuated rectangular chamber [73]), i.e., a significantly visible v_2 field. However, due to the inability to model such complex 3D flows, we do not include the effect of a streaming field on the particle's motion in our comparative analysis later in Sec. III B.

Nevertheless, it is informative to address the qualitative effects of a steady flow field in the y direction on the particle's motion. The effect of the u_2 and w_2 fields on the particle's motion have been discussed in Sec. III A 1. To obtain a qualitative idea of how a v_2 streaming field would affect the collection lengths, we separately model the movement of a particle by including a hypothetical v_2 field. The hypothetical v_2 field is assumed to have a spatial variation in x and z similar to those of the w_2 and the u_2 fields, respectively, and to remain constant in the y direction. The magnitude of this v_2 streaming field is varied through a factor s, where at $s = 1$ the magnitude of the v_2 field is equal to that of the u_2 field; s is varied from 0 to 2 as shown in Table II. The collection length of the particles in the above-mentioned hypothetical streaming field, obtained over a range of flow rates, is fitted with a power curve ($L_c \propto Q^b$) and the exponent b of the same is listed in Table II.

The table clearly depicts that the trend of the collection length against the flow rate is significantly affected by the v_2 streaming field. Although these variations are not physically derived, the data is useful for corroboration with experiments and is used, in the next section, to help explain the deviations in the experimentally observed collection lengths with those from the simulations. Furthermore, despite the simplifications, the model provides a quantitative evaluation of the relative effects of the inlet-induced transverse fields and capillary-wave-induced fields on particle motion, thereby informing better system design.

B. Experiments

The collection profile of particles in the channel as observed experimentally is shown in Fig. 6. In agreement with the simulations, the particles are seen to first diverge from the inlet, due to the dominant drag force from the inlet-induced transverse flow. Then, further downstream, the particles converge toward the center of the channel because of the dominant collection forces from the capillary-wave excitation.

The operating frequency is identified by a frequency sweep. As mentioned in Sec. II A 2, the resonant frequency is identified by a peak in the capillary-wave displacement amplitude during a frequency sweep. As the vibration amplitude is low, capillary waves are not visible on the water-air interface with the naked eye. However, the peak in the capillary-wave displacement is observed in the form of the collection length L_c. As the collection force (F_{eq}) depends on the velocity-field magnitude ($F_{eq} \propto |\mathbf{u}|^2$), the collection force would also peak at the resonant frequency, thereby leading to a minimum in the collection length.

The collection shown in Fig. 6(a) is obtained at a frequency of 13 Hz, which is close to the theoretical frequency of a capillary wave of one wavelength across the 8 mm width [12.9 Hz from Eq. (8)]. However, this collection is affected by any wave formed along the y direction. As such, any misalignment in mounting the device or geometric irregularities along the edge of the channel can give rise to perturbations along the y direction, resulting in a capillary wave. An example of this is observed in Fig. 6(b), where the channel is vibrated at 15 Hz, close to the theoretical frequency of a capillary wave of four wavelengths along the channel length [15.5 Hz from Eq. (8) for $L = 30$ mm]. The collection profile is observed to have been distorted, which can be attributed to the interference of the capillary wave along the y direction. Additionally, no particle collection is observed below a frequency of 10 Hz. The channel geometry shown in Fig. 6 is solely to illustrate that the particles converge and exit from the central

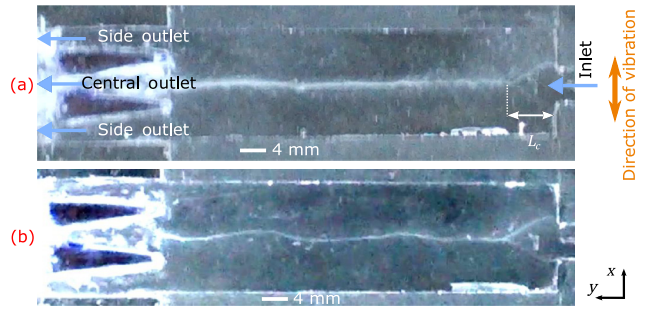

FIG. 6. (a) The movement of silica particles ($d = 5$ μm) along the channel as observed in experiments at a frequency of 13 Hz. (b) The particle motion at 15 Hz shows a wavy particle-collection line along y due to the interaction of the capillary wave along y.

outlet only. However, for further experiments, the channel geometry shown in Fig. 2(e) is employed, which eases the separation of the particle concentrate (central outlet) and the filtrate (side outlet). The filtrate is then scanned for particles using DLS to validate the absence of particles from the side outlets.

Figure 7 shows a comparison of the collection length observed from experiments with those obtained from simulations for different inlet widths and flow rates. The variation of L_c with the flow rate and the inlet width is in line with the discussion in Sec. III A 2. Smaller inlet widths lead to a higher particle concentration near the centerline of the channel while competing with an increasing F_{dx}, which results in the trend shown in Fig. 7(e). A further decrease in the inlet width is accompanied by the formation of vortices near the inlet, which increases the collection length. An increase in the flow rate also determines the formation of such vortices [75], thereby restricting the maximum operating flow rate. Furthermore, the upper limit on the flow rate is also restricted by the condition of ensuring a connected liquid volume between the inlet and the outlet (Sec. II A 1). Finally, extremely low flow rates are also not advised, as they may cause particle accumulation at the inlet due to solid friction on the particles from the channel base.

It is observed from Fig. 7 that the simulation results agree with the experiments to varying degrees. As discussed in Sec. II A 4, the present model incorporates several assumptions in order to tackle the modeling of this complex 3D flow field. Specifically, the assumptions related to the noninclusion of only a 2D streaming field, neglecting the v_2 flows (in the third dimension) and its subsequent effect on the u_2 and w_2, is a significant source of error in the simulation results. In particular, the v_2 field will influence the variation of collection length. To investigate the effect of v_2 on the collection length, Table III compares the variation of L_c with Q for the data from experiments with those obtained from simulations with streaming for the case $s = 1$, as explained in Sec. III A 2. and Table II. Table III also provides a comparison between the trends from experiments and with simulations without streaming (the current simulation model setup). The trend of L_c vs Q from experiments shows a clear departure from the simulations without streaming, but seems to closely follow the trend from simulations where a hypothetical streaming in y is considered. Again, as mentioned in Sec. III A 2, the analysis considering the inclusion of streaming fields is only intended to be indicative of the effects of streaming.

Figure 8(a) shows the collection lengths for silica particles in a channel of width 8 mm for varying actuation amplitudes. An increase in the actuation amplitude increases the collection forces, thereby decreasing the collection length. However, it has to be mentioned that higher amplitudes also increase the streaming-field strength, thereby increasing the chances of an incomplete collection. The highest amplitude employed in the experiments is 500 μm at 13 Hz, for two reasons: (1) a higher-amplitude capillary-wave movement hinders a clear observation of particle collection and (2) the chances of liquid spillage from the sides are increased. As was mentioned in Sec. II A 4, the inlet-induced transverse flow field can be

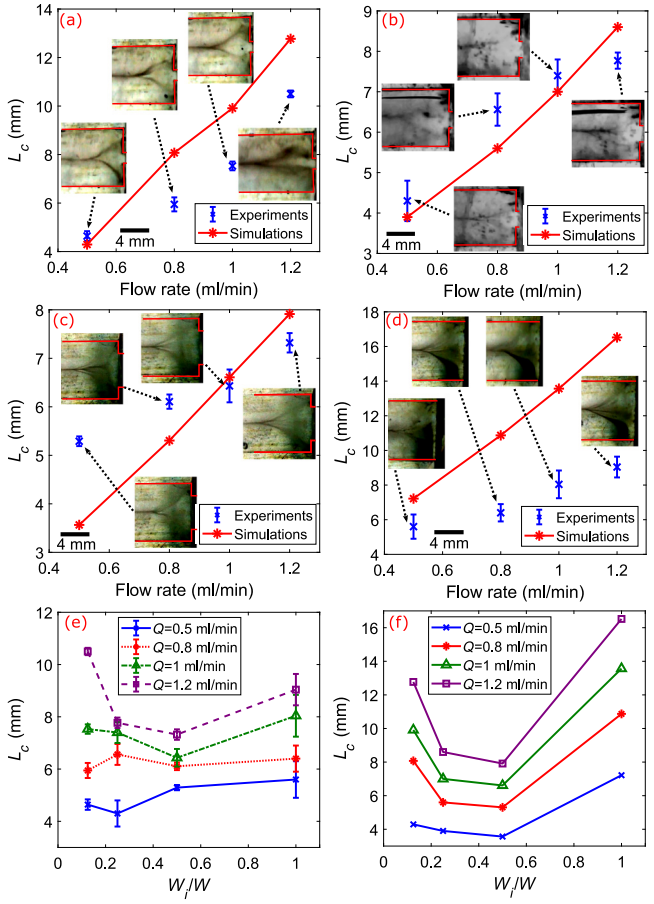

FIG. 7. The collection length, for silica particles ($d = 5$ μm), in a channel of width 8 mm with varying Q at $f = 13$ Hz and $A_0 = 220$ μm: (a) $W_i = 1$ mm; (b) $W_i = 2$ mm; (c) $W_i = 4$ mm; (d) $W_i = 8$ mm. (e),(f) The variation of L_c with W_i/W from (e) experiments and (f) simulations.

TABLE III. A comparison of the exponent b of $L_c \propto Q^b$ between experiments and simulations. The table compares data from simulations with no streaming, simulations with a streaming field (assuming v_2 field with $s = 1$ from Table II), and experiments.

	Simulations		
W_i (mm)	No streaming	$s = 1$	Experiments
1	1.21	1.18	1.05
2	0.94	0.74	0.64
4	0.93	0.58	0.36
8	0.97	0.58	0.59

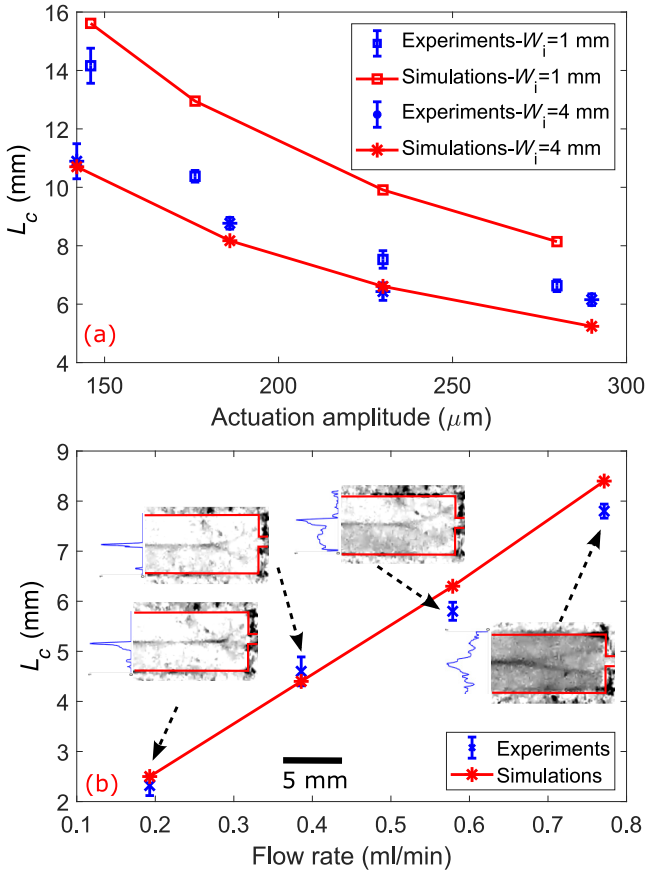

FIG. 8. (a) The collection length L_c of silica particles ($d = 5\ \mu$m) in a channel of width 8 mm with varying A_0 for different W_i at $f = 13$ Hz and $Q = 1$ ml/min. (b) The collection length of silica particles in a channel of width 5 mm for varying Q at $f = 22$ Hz ($W_i = 1.6$ mm, $A_0 = 86\ \mu$m): the normalized particle distribution along the channel width is also shown.

expected to be time-periodic, due to the vibrating liquid-air interface. Therefore, the transverse flow will also contribute to the streaming-field strength, thereby affecting the cutoff characteristics, which implies that the flow rate Q will also affect the cutoff characteristics of the system. The same is observed in Fig. 8(b), which shows the particle-collection profile of silica particles of diameter 5 μm in a channel with width 5 mm ($f = 23$ Hz). Due to the narrower channel width, the particles are more susceptible to the streaming flows compared to the 8-mm-wide channel [74]. Therefore, these channels are more sensitive to changes in parameters that affect the streaming-field strength. At low flow rates, the collection seems to be complete—the observations are supported by DLS measurements—while at increased flow rates, particles can be seen across the channel [observed as a hazy liquid as well as through the image intensity distributions in Fig. 8(b)], implying an incomplete collection.

Figure 9 shows the nondimensionalized plots based on Eq. (18) for the data corresponding to the 5 μm silica

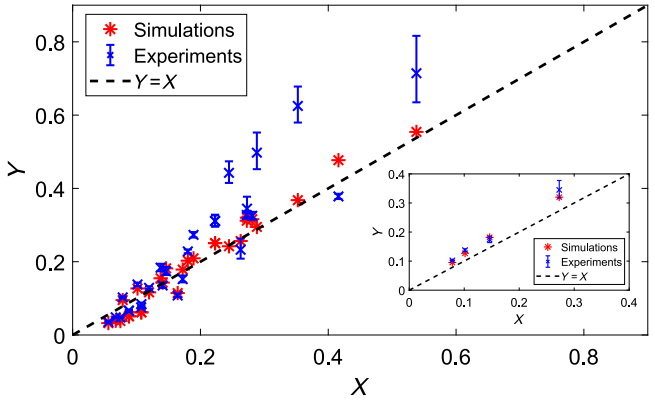

FIG. 9. A comparison of experimental and numerical data nondimensionalized as per Eqs. (19a) and (19b) for all the cases shown in Figs. 7 and 8. The inset specifically shows the data points for the experiments with channel width 5 mm from Fig. 8(b).

particles, where

$$X = \frac{W_i}{2L_c}, \tag{19a}$$

$$Y = 0.08\frac{A_n^{0.1}}{Q_n^{0.9}}(2.9 + 11.7r_n - 134.9r_n^2) - 0.15\frac{A_n^{0.2}}{Q_n^{0.8}}\left(1 - \frac{W_i}{W}\right)^2(2.1 + 17.4r_n - 137.4r_n^2). \tag{19b}$$

Figure 9 does not contain data for 1 μm polystyrene particles as shown in Fig. 10(a), because Eq. (18) is valid only for the particle size range mentioned in Table I. A particle's motion in the z direction is determined by a balance between the drag force (F_{dz}) and its weight (F_w). Lower particle sizes experience an increased effect of the drag force compared to the particle's weight ($F_{dz}/F_w \propto 1/r$), allowing the particle to remain dislodged from the base for longer times, as shown in Fig. 10(b). As the flow fields are much stronger at higher z (Fig. 3), lighter particles travel a longer distance before sedimenting and thereby exhibit an altered interaction with the flow fields compared to the heavier particles. Although Eq. (18) is unable to predict the collection length for particles of sizes 1 μm, the simulation procedure employed in this work (discussed in Sec. II A) is able to predict the collection lengths with a fair bit of accuracy, as seen in Fig. 10(a).

As explained above, the two types of particles used in the present work demonstrate different movement characteristics during their collection, wherein the collection lengths can be reasonably predicted by the simulation procedure. Smaller (or lighter) particle sizes are strongly affected by the streaming field, causing them to swirl and

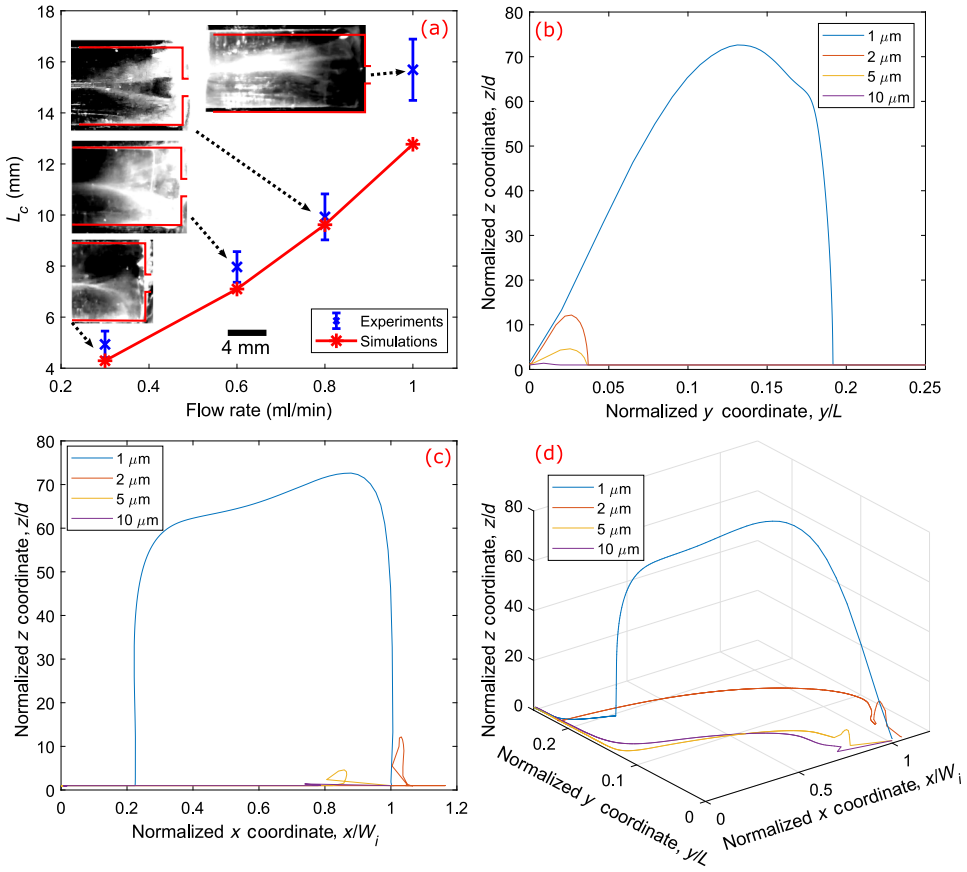

FIG. 10. (a) The collection length for polystyrene particles ($d = 1$ μm) with varying Q at $f = 13$ Hz, $A_0 = 220$ μm, in a channel with $W = 8$ mm and $W_i = 2$ mm. (b),(c),(d) A comparison of the motion of different particle sizes from simulations in (b) the y-z plane, (c) the x-z plane, (d) 3D motion. The particle motion shown here represents the position of the particle at the end of each cycle.

disperse in the liquid bulk, rather than collecting stably, while larger (or heavier) particles show collection characteristics similar to the silica particles. In such a case, theoretical estimates suggest that the collection length does not significantly depend on the particle size. Looking at Eq. (17), the collection length is primarily a competition between the drag force due to the inlet-induced transverse flow ($F_{dx} = 6\pi\mu ru$) and the vibration-induced collection forces (F_{eq}). F_{eq} varies as roughly $r^{1.7}$ from simulations on horizontal excitation of a rectangular-cross-section chamber [70], while experimentally this is observed to be about $r^{1.4}$ for particle sizes ranging from 3 μm to 40 μm. The drag force due to the inlet-induced transverse velocity field (F_{dx}) varies close to r^2, accounting for the increase

TABLE IV. A summary of the limits on actuation and on the flow parameters for designing a system for collecting particles using the proposed capillary-wave-based method.

Parameter	Effect of increase in parameter	Upper limit	Lower limit
W_i	Decreased F_{dx} and F_{dy} near inlet: variable effect on L_c	$W_i = W$	Vortex formation near inlet [75]
Q	Increased F_{dx} and F_{dy}: increased L_c	Streaming trap, $L_c < L$, connected inlet and outlet, jetting at the inlet	Particle accumulation at inlet
A_0	Increased F_{eq} and streaming: decreased L_c	Streaming trap	$L_c < L$
L	No significant effect on F_{eq}, F_{dx}, or F_{dy}	Capillary breakup [80]	$L_c < L$
W	Decreased F_{eq} and streaming: increased L_c	$L_c < L$	Streaming trap
h	No effect on F_{eq}, increased streaming	Streaming trap, $h < \lambda$ [69]	Boundary to confine liquid in the rectangular channel

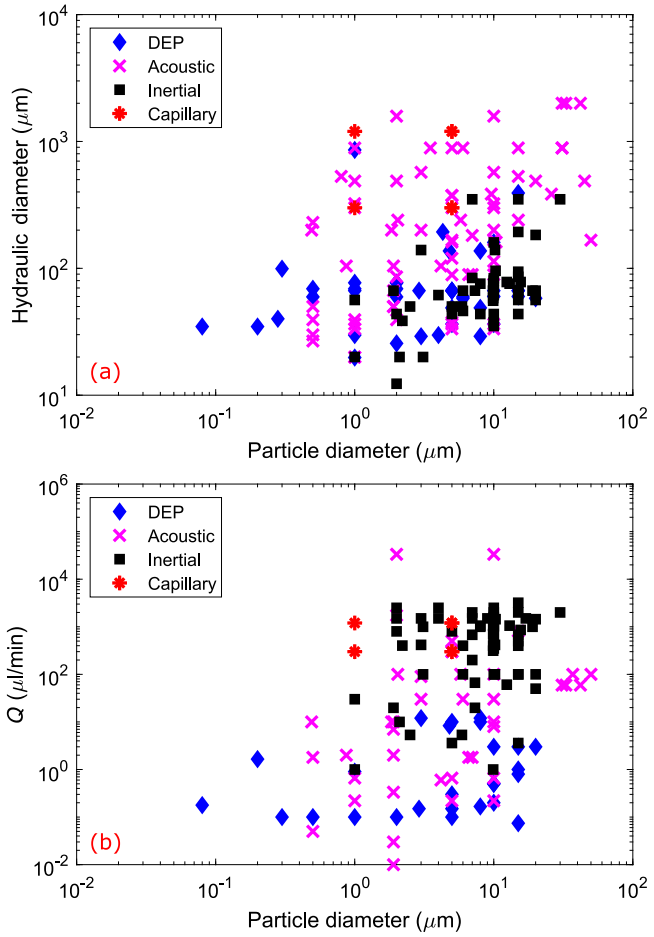

FIG. 11. A comparison of the proposed capillary-wave-based microparticle-collection method with different microfluidic particle-collection schemes: (a) the hydraulic diameter of the channel plotted against the particle diameter; (b) the flow rate plotted against the particle diameter. The data points included in the graphs have been extracted from the following references: inertial microfluidics [5,83–112], acoustics [23,26,44,45,47,48,113–126] and dielectrophoresis (DEP) [127–142].

in velocity-flow magnitude with increasing particle radius near the base. The above explanation shows a faint dependency of the particle sizes on the collection length ($r^{0.6}$). This weak dependency is further supported by the simulation data [from Eq. (18)], where for a 50% change in the radius (from 5 μm), the collection length changes by less than 5%, which would not be differentiable experimentally. In comparison, other parameters such as the channel width (W), the inlet width (W_i), the actuation amplitude (A_0), and the flow rate (Q) show much stronger effects on the collection length (greater than 40%).

Table IV qualitatively summarizes the design criteria for designing a channel for continuous particle collection considering geometrical, flow stability, and streaming limitations on particle movement. It is also informatory to evaluate the collection characteristics of this capillary-wave-based method with other particle-manipulation methods. Figure 11 provides a comparison of this method with three predominantly employed microscale continuous flow methods for microparticle collection. The figure compares the reported particle sizes collected by the respective actuation mechanisms with the hydraulic diameter of the channel and the maximum reported flow rates.

The data presented in Fig. 11 for the capillary case are presently limited to particle sizes of 1 μm only. Considering the capabilities of the batch manipulation system explored in our previous study [72], the present system provides the possibility of manipulating submicron-sized particles. As the streaming-field strength increases and the collection forces decrease with decreasing particle sizes [74], the proposed collection device will be efficient at larger channel widths and lower vibration amplitudes (which correspond to lower-magnitude streaming fields) and also at lower operating flow rates (to compensate for the lower collection forces).

IV. CONCLUSION

Continuous focusing of microparticles is demonstrated in an open water-filled rectangular-cross-section channel subjected to low-frequency periodic vibrations. This capillary-wave-based particle manipulation mechanism is known to collect particles underneath the nodes of the capillary wave in a batch operation mode [72]. The present work expands the capability of this collection mechanism to continuously collect microparticles at flow rates up to 1.2 ml/min. A numerical model is proposed which traces the motion of a particle by superimposing a 2D flow field due to the periodic vibrations (which affects the collection) with a steady 3D flow field (driving particle movement from inlet to outlet). Although the model contains inaccuracies, it provides a fair estimation of the length from the inlet at which particles converge into a focused stream. The effects of vibration amplitude, channel dimensions, and channel inlet widths on the collection length and collection quality are discussed through simulations and experimental observations. The effect of the streaming field on the deviation between simulation and experimental results is also discussed. Finally, based on the simulation model and experimental observations, parameters pertaining to channel design and actuation are summarized considering effects on fluid flow and particle motion. With the advantages of a simple setup and operation, the proposed methodology demonstrates an alternative to achieve continuous focusing of microparticles with flow rates comparable to existing microfluidics-based particle-collection schemes.

ACKNOWLEDGMENTS

The authors would like to thank Professor Rochish Thaokar of the Department of Chemical Engineering,

Indian Institute of Technology, Bombay for providing access to the DLS equipment. The authors would also like to acknowledge Mr. Raj Mashruwala for his generous donation to allow the research work to be carried out in the Suman Mashruwala Advance Microengineering Laboratory, Department of Mechanical Engineering, Indian Institute of Technology, Bombay.

[1] J. F. Richardson, J. H. Harker, and J. R. Backhurst, *Particle Technology and Separation Processes* (Butterworth-Heinemann, Woburn, MA, 2002).

[2] Torsten Vilkner, Dirk Janasek, and Andreas Manz, Micro total analysis systems: Recent developments, Anal. Chem. **76**, 3373 (2004).

[3] David W. Inglis, John A. Davis, Robert H. Austin, and James C. Sturm, Critical particle size for fractionation by deterministic lateral displacement, Lab Chip **6**, 655 (2006).

[4] David W. Inglis and Nick Herman, A scalable approach for high throughput branch flow filtration, Lab Chip **13**, 1724 (2013).

[5] Dino Di Carlo, Daniel Irimia, Ronald G. Tompkins, and Mehmet Toner, Continuous inertial focusing, ordering, and separation of particles in microchannels, Proc. Natl. Acad. Sci. **104**, 18892 (2007).

[6] Abhishek Jain and Jonathan D. Posner, Particle dispersion and separation resolution of pinched flow fractionation, Anal. Chem. **80**, 1641 (2008).

[7] Arun T. J. Kadaksham, Pushpendra Singh, and Nadine Aubry, Dielectrophoresis of nanoparticles, Electrophoresis **25**, 3625 (2004).

[8] C. Mio, T. Gong, A. Terray, and D. W. M. Marr, Design of a scanning laser optical trap for multiparticle manipulation, Rev. Sci. Instrum. **71**, 2196 (2000).

[9] Q. Cao, X. Han, and L. Li, Two-dimensional manipulation of magnetic nanoparticles in microfluidic systems, Appl. Phys. Express **6**, 025201 (2013).

[10] H. M. Hertz, Standing wave acoustic trap for nonintrusive positioning of microparticles, J. Appl. Phys. **78**, 4845 (1995).

[11] P. Sajeesh and AshisKumar Sen, Particle separation and sorting in microfluidic devices: A review, Microfluid. Nanofluidics **17**, 1 (2014).

[12] Xiangchun Xuan, Junjie Zhu, and Christopher Church, Particle focusing in microfluidic devices, Microfluid. Nanofluidics **9**, 1 (2010).

[13] Henrik Bruus, Acoustofluidics 2: Perturbation theory and ultrasound resonance modes, Lab Chip **12**, 20 (2012).

[14] A. Garcia-Sabaté, A. Castro, M. Hoyos, and R. González-Cinca, Experimental study on inter-particle acoustic forces, J. Acoust. Soc. Am. **135**, 1056 (2014).

[15] L. Rayleigh, On the circulation of air observed in Kundt's tubes, and on some allied acoustical problems, Phil. Trans. R. Soc. London **175**, 1 (1884).

[16] August Kundt, Ueber eine neue Art Akustischer Staubfiguren und ber die Anwendung derselben zur Bestimmung der Schallgeschwindigkeit in festen Körpern und Gasen, Ann. Phys. **203**, 497 (1866).

[17] J. Greenhall, F. Guevara Vasquez, and B. Raeymaekers, Continuous and unconstrained manipulation of micro-particles using phase-control of bulk acoustic waves, Appl. Phys. Lett. **103**, 074103 (2013).

[18] C. Devendran, I. Gralinski, and A. Neild, Separation of particles using acoustic streaming and radiation forces in an open microfluidic channel, Microfluid. Nanofluidics **17**, 879 (2014).

[19] A. Grinenko, C. K. Ong, C. R. P. Courtney, P. D. Wilcox, and B. W. Drinkwater, Efficient counter-propagating wave acoustic micro-particle manipulation, Appl. Phys. Lett. **101**, 233501 (2012).

[20] Helen Mulvana, Sandy Cochran, and Martyn Hill, Ultrasound assisted particle and cell manipulation on-chip, Adv. Drug Deliv. Rev. **65**, 1600 (2013).

[21] Thomas Schwarz, Guillaume Petit-Pierre, and Jurg Dual, Rotation of non-spherical micro-particles by amplitude modulation of superimposed orthogonal ultrasonic modes, J. Acoust. Soc. Am. **133**, 1260 (2013).

[22] Leslie Y. Yeo and James R. Friend, Ultrafast microfluidics using surface acoustic waves, Biomicrofluidics **3**, 012002 (2009).

[23] Linda Johansson, Johannes Enlund, Stefan Johansson, Ilia Katardjiev, and Ventsislav Yantchev, Surface acoustic wave induced particle manipulation in a PDMS channel—principle concepts for continuous flow applications, Biomed. Microdevices **14**, 279 (2012).

[24] Priscilla R. Rogers, James R. Friend, and Leslie Y. Yeo, Exploitation of surface acoustic waves to drive size-dependent microparticle concentration within a droplet, Lab Chip **10**, 2979 (2010).

[25] D. J. Collins, B. Morahan, J. Garcia-Bustos, C. Doerig, M. Plebanski, and A. Neild, Two-dimensional single-cell patterning with one cell per well driven by surface acoustic waves, Nat. Commun. **6**, 8686 (2015).

[26] David J. Collins, Tuncay Alan, and Adrian Neild, Particle separation using virtual deterministic lateral displacement (vDLD), Lab Chip **14**, 1595 (2014).

[27] T. Franke, S. Braunmuller, L. Schmid, A. Wixforth, and D. A. Weitz, Surface acoustic wave actuated cell sorting (SAWACS), Lab Chip **10**, 789 (2010).

[28] Xiaoyun Ding, Peng Li, Sz-Chin Steven Lin, Zackary S. Stratton, Nitesh Nama, Feng Guo, Daniel Slotcavage, Xiaole Mao, Jinjie Shi, Francesco Costanzo, and Tony Jun Huang, Surface acoustic wave microfluidics, Lab Chip **13**, 3626 (2013).

[29] Yuchao Chen, Ahmad Ahsan Nawaz, Yanhui Zhao, Po-Hsun Huang, J. Phillip McCoy, Stewart J. Levine, Lin Wang, and Tony Jun Huang, Standing surface acoustic wave (SSAW)-based microfluidic cytometer, Lab Chip **14**, 916 (2014).

[30] L. P. Gor'kov, On the forces acting on a small particle in an acoustical field in an ideal fluid, Sov. Phys.-Dokl. **6**, 773 (1962).

[31] Louis V. King, On the acoustic radiation pressure on spheres, Proc. R. Soc. Lond. A: Math. Phys. Eng. Sci. **147**, 212 (1934).

[32] R. Jensen, I. Gralinski, and A. Neild, Ultrasonic manipulation of particles in an open fluid film, IEEE Trans. Ultrason. Ferroelectr. Freq. Control **60**, 1964 (2013).

[33] S. Oberti, A. Neild, R. Quach, and J. Dual, The use of acoustic radiation forces to position particles within fluid droplets, Ultrasonics **49**, 47 (2009).

[34] Charles R. P. Courtney, Bruce W. Drinkwater, Christine E. M. Demore, Sandy Cochran, Alon Grinenko, and Paul D. Wilcox, Dexterous manipulation of microparticles using Bessel-function acoustic pressure fields, Appl. Phys. Lett. **102**, 123508 (2013).

[35] P. Glynne-Jones, R. J. Boltryk, N. R. Harris, A. W. J. Cranny, and M. Hill, Mode-switching: A new technique for electronically varying the agglomeration position in an acoustic particle manipulator, Ultrasonics **50**, 68 (2010).

[36] Alon Grinenko, Paul D. Wilcox, Charles R. P. Courtney, and Bruce W. Drinkwater, Proof of principle study of ultrasonic particle manipulation by a circular array device, Proc. R. Soc. A **468**, 3571 (2012).

[37] Myeong Chan Jo and Rasim Guldiken, Particle manipulation by phase-shifting of surface acoustic waves, Sens. Actuators A: Phys. **207**, 39 (2014).

[38] Jinjie Shi, Daniel Ahmed, Xiaole Mao, Sz-Chin Steven Lin, Aitan Lawit, and Tony Jun Huang, Acoustic tweezers: Patterning cells and microparticles using standing surface acoustic waves (SSAW), Lab Chip **9**, 2890 (2009).

[39] R. D. O'Rorke, C. D. Wood, C. Wälti, S. D. Evans, A. G. Davies, and J. E. Cunningham, Acousto-microfluidics: Transporting microbubble and microparticle arrays in acoustic traps using surface acoustic waves, J. Appl. Phys. **111**, 094911 (2012).

[40] C. D. Wood, J. E. Cunningham, R. O'Rorke, C. Wälti, E. H. Linfield, A. G. Davies, and S. D. Evans, Formation and manipulation of two-dimensional arrays of micron-scale particles in microfluidic systems by surface acoustic waves, Appl. Phys. Lett. **94**, 054101 (2009).

[41] Marco Travagliati, Richie J. Shilton, Marco Pagliazzi, Ilaria Tonazzini, Fabio Beltram, and Marco Cecchini, Acousto fluidics and whole-blood manipulation in surface acoustic wave counterflow devices, Anal. Chem. **86**, 10633 (2014).

[42] S. Oberti, D. Moeller, A. Neild, J. Dual, F. Beyeler, B. J. Nelson, and S. Gutmann, Strategies for single particle manipulation using acoustic and flow fields, Ultrasonics **50**, 247 (2010).

[43] M. Antfolk, P. B. Muller, P. Augustsson, H. Bruus, and T. Laurell, Focusing of sub-micrometer particles and bacteria enabled by two-dimensional acoustophoresis, Lab Chip **14**, 2791 (2014).

[44] E. J. Fong, A. C. Johnston, T. Notton, S.-Y Jung, K. A. Rose, L. S. Weinberger, and M. Shusteff, Acoustic focusing with engineered node locations for high-performance microfluidic particle separation, Analyst **139**, 1192 (2014).

[45] Takahiro Kanazaki and Tetsuo Okada, Two-dimensional particle separation in coupled acoustic-gravity-flow field vertically by composition and laterally by size, Anal. Chem. **84**, 10750 (2012).

[46] Yang Liu and Kian-Meng Lim, Particle separation in microfluidics using a switching ultrasonic field, Lab Chip **11**, 3167 (2011).

[47] Filip Petersson, Andreas Nilsson, Cecilia Holm, Henrik Jonsson, and Thomas Laurell, Continuous separation of lipid particles from erythrocytes by means of laminar flow and acoustic standing wave forces, Lab Chip **5**, 20 (2005).

[48] Jeonghun Nam, Yongjin Lee, and Sehyun Shin, Size-dependent microparticles separation through standing surface acoustic waves, Microfluid. Nanofluidics **11**, 317 (2011).

[49] M. Ohlin, A. E. Christakou, T. Frisk, B. Önfelt, and M. Wiklund, Influence of acoustic streaming on ultrasonic particle manipulation in a 100-well ring-transducer microplate, J. Micromech. Microeng. **23**, 035008 (2013).

[50] Rune Barnkob, Per Augustsson, Thomas Laurell, and Henrik Bruus, Acoustic radiation- and streaming-induced microparticle velocities determined by microparticle image velocimetry in an ultrasound symmetry plane, Phys. Rev. E **86**, 056307 (2012).

[51] A. L. Bernassau, P. Glynne-Jones, F. Gesellchen, M. Riehle, M. Hill, and D. R. S. Cumming, Controlling acoustic streaming in an ultrasonic heptagonal tweezers with application to cell manipulation, Ultrasonics **54**, 268 (2014).

[52] Kenneth D. Frampton, Shawn E. Martin, and Keith Minor, The scaling of acoustic streaming for application in microfluidic devices, Appl. Acoust. **64**, 681 (2003).

[53] J. F. Spengler, W. T. Coakley, and K. T. Christensen, Microstreaming effects on particle concentration in an ultrasonic standing wave, AIChE J. **49**, 2773 (2003).

[54] Mark F. Hamilton, Yurii A. Ilinskii, and Evgenia A. Zabolotskaya, Acoustic streaming generated by standing waves in two-dimensional channels of arbitrary width, J. Acoust. Soc. Am. **113**, 153 (2003).

[55] Daniel Ahmed, Xiaole Mao, Jinjie Shi, Bala Krishna Juluri, and Tony Jun Huang, A millisecond micromixer via single-bubble-based acoustic streaming, Lab Chip **9**, 2738 (2009).

[56] James Collis, Richard Manasseh, Petar Liovic, Paul Tho, Andrew Ooi, Karolina Petkovic-Duran, and Yonggang Zhu, Cavitation microstreaming and stress fields created by microbubbles, Ultrasonics **50**, 273 (2010). Note selected Papers from {ICU} 2009

[57] K. Sritharan, C. J. Strobl, M. F. Schneider, A. Wixforth, and Z. Guttenberg, Acoustic mixing at low Reynolds numbers, Appl. Phys. Lett. **88**, 054102 (2006).

[58] K. Petkovic-Duran, R. Manasseh, Y. Zhu, and A. Ooi, Chaotic micromixing in open wells using audio-frequency acoustic microstreaming, Bio Techniques **47**, 827 (2009).

[59] Kwitae Chong, Scott D. Kelly, Stuart Smith, and Jeff D. Eldredge, Inertial particle trapping in viscous streaming, Phys. Fluids **25**, 033602 (2013).

[60] T. A. House, V. H. Lieu, and D. T. Schwartz, A model for inertial particle trapping locations in hydrodynamic tweezers arrays, J. Micromech. Microeng. **24**, 045019 (2014).

[61] Barry R. Lutz, Jian Chen, and Daniel T. Schwartz, Hydrodynamic tweezers: 1. Noncontact trapping of single cells using steady streaming microeddies, Anal. Chem. **78**, 5429 (2006).

[62] Priscilla Rogers and Adrian Neild, Selective particle trapping using an oscillating microbubble, Lab Chip **11**, 3710 (2011).

[63] Maulik V. Patel, Imaly A. Nanayakkara, Melinda G. Simon, and Abraham P. Lee, Cavity-induced microstreaming for simultaneous on-chip pumping and size-based separation of cells and particles, Lab Chip **14**, 3860 (2014).
[64] P. Rogers, I. Gralinski, C. Galtry, and A. Neild, Selective particle and cell clustering at air-liquid interfaces within ultrasonic microfluidic systems, Microfluid. Nanofluidics **14**, 469 (2013).
[65] D. Klotsa, Michael R. Swift, R. M. Bowley, and P. J. King, Chain formation of spheres in oscillatory fluid flows, Phys. Rev. E **79**, 021302 (2009).
[66] D. Klotsa, Michael R. Swift, R. M. Bowley, and P. J. King, Interaction of spheres in oscillatory fluid flows, Phys. Rev. E **76**, 056314 (2007).
[67] S. Lukaschuk, P. Denissenko, and G. Falkovich, Nodal patterns of floaters in surface waves, Eur. Phys. J. Spec. Top. **145**, 125 (2007).
[68] J. Whitehill, A. Neild, T. W. Ng, and M. Stokes, Collection of suspended particles in a drop using low frequency vibration, Appl. Phys. Lett. **96**, 053501 (2010).
[69] P. Agrawal, P. S. Gandhi, and A. Neild, The mechanics of microparticle collection in an open fluid volume undergoing low frequency horizontal vibration, J. Appl. Phys. **114**, 114904 (2013).
[70] P. Agrawal, P. S. Gandhi, and A. Neild, Quantification and comparison of low frequency microparticle collection mechanism in an open rectangular chamber, J. Appl. Phys. **115**, 174505 (2014).
[71] J. D. Whitehill, I. Gralinski, D. Joiner, and A. Neild, Nanoparticle manipulation within a microscale acoustofluidic droplet, J. Nanopart. Res. **14**, 1223 (2012).
[72] Prashant Agrawal, Prasanna S. Gandhi, and Adrian Neild, Microparticle Response to Two-Dimensional Streaming Flows in Rectangular Chambers Undergoing Low-Frequency Horizontal Vibrations, Phys. Rev. Applied **2**, 064008 (2014).
[73] Prashant Agrawal, Prasanna S. Gandhi, and Adrian Neild, Particle manipulation affected by streaming flows in vertically actuated open rectangular chambers, Phys. Fluids **28**, 032001 (2016).
[74] Prashant Agrawal, Prasanna S. Gandhi, and Adrian Neild, Frequency effects on microparticle motion in horizontally actuated open rectangular chambers, Microfluid. Nanofluidics **19**, 1209 (2015).
[75] Jue Nee Tan, Tuncay Alan, and Adrian Neild, Stability of flowing open fluidic channels, AIP Adv. **3**, 022121 (2013).
[76] L. D. Landau and E. M. Lifshitz, *Fluid Mechanics* (Pergamon Press, Oxford, 1987).
[77] W. L. M. Nyborg, *Physical Acoustics IIB* (Academic Press, New York, 1965).
[78] R. Clift, J. R. Grace, and M. E. Weber, *Bubbles, Drops, and Particles* (Academic Press, New York, 1978).
[79] A. J. Goldman, R. G. Cox, and H. Brenner, Slow viscous motion of a sphere parallel to a plane wall—II Couette flow, Chem. Eng. Sci. **22**, 653 (1967).
[80] Anton A. Darhuber, Sandra M. Troian, Scott M. Miller, and Sigurd Wagner, Morphology of liquid microstructures on chemically patterned surfaces, J. Appl. Phys. **87**, 7768 (2000).
[81] J. W. Gibbs, *The Scientific Papers of J. Willard Gibbs* (Longmans, Green and Company, London, 1906).
[82] Jiansheng Feng and Jonathan P. Rothstein, One-way wicking in open micro-channels controlled by channel topography, J. Colloid Interface Sci. **404**, 169 (2013).
[83] Jun Zhang, Sheng Yan, Gursel Alici, Nam-Trung Nguyen, Dino Di Carlo, and Weihua Li, Real-time control of inertial focusing in microfluidics using dielectrophoresis (DEP), RSC Adv. **4**, 62076 (2014).
[84] Seungjeong Song and Sungyoung Choi, Inertial modulation of hydrophoretic cell sorting and focusing, Appl. Phys. Lett. **104**, 074106 (2014).
[85] Jian Zhou, Premkumar Vummidi Giridhar, Susan Kasper, and Ian Papautsky, Modulation of aspect ratio for complete separation in an inertial microfluidic channel, Lab Chip **13**, 1919 (2013).
[86] Vahidreza Parichehreh and Palaniappan Sethu, Inertial lift enhanced phase partitioning for continuous microfluidic surface energy based sorting of particles, Lab Chip **12**, 1296 (2012).
[87] Kyung Won Seo, Yong Seok Choi, and Sang Joon Lee, Dean-coupled inertial migration and transient focusing of particles in a curved microscale pipe flow, Exp. Fluids **53**, 1867 (2012).
[88] Daniel R. Gossett and Dino Di Carlo, Particle focusing mechanisms in curving confined flows, Anal. Chem. **81**, 8459 (2009).
[89] I. D. Johnston, M. B. McDonnell, C. K. L. Tan, D. K. McCluskey, M. J. Davies, and M. C. Tracey, Dean flow focusing and separation of small microspheres within a narrow size range, Microfluid. Nanofluidics **17**, 509 (2014).
[90] Ali Asgar S. Bhagat, Sathyakumar S. Kuntaegowdanahalli, and Ian Papautsky, Continuous particle separation in spiral microchannels using Dean flows and differential migration, Lab Chip **8**, 1906 (2008).
[91] Ali Asgar S. Bhagat, Sathyakumar S. Kuntaegowdanahalli, Necati Kaval, Carl J. Seliskar, and Ian Papautsky, Inertial microfluidics for *sheath-less* high-throughput flow cytometry, Biomed. Microdevices **12**, 187 (2010).
[92] X. Zhang, A. S. Kim, and D. Garmire, Particle-train dynamics in curved microfluidic channels at intermediate Reynolds numbers, Chem. Eng. Sci. **98**, 69 (2013).
[93] Joseph M. Martel and Mehmet Toner, Inertial focusing dynamics in spiral microchannels, Phys. Fluids (1994-present) **24**, 032001 (2012).
[94] Tae Hyun Kim, Hyeun Joong Yoon, Philip Stella, and Sunitha Nagrath, Cascaded spiral microfluidic device for deterministic and high purity continuous separation of circulating tumor cells, Biomicrofluidics **8**, 064117 (2014).
[95] J. Zhang, M. Li, W. H. Li, and G. Alici, Inertial focusing in a straight channel with asymmetrical expansion-contraction cavity arrays using two secondary flows, J. Micromech. Microeng. **23**, 085023 (2013).
[96] Kazuma Miura, Tomoaki Itano, and Masako Sugihara-Seki, Inertial migration of neutrally buoyant spheres in a pressure-driven flow through square channels, J. Fluid Mech. **749**, 320 (2014).
[97] Chao Liu, Guoqing Hu, Xingyu Jiang, and Jiashu Sun, Inertial focusing of spherical particles in rectangular

microchannels over a wide range of Reynolds numbers, Lab Chip **15**, 1168 (2015).

[98] Yong-Seok Choi, Kyung-Won Seo, and Sang-Joon Lee, Lateral and cross-lateral focusing of spherical particles in a square microchannel, Lab Chip **11**, 460 (2011).

[99] Seungyoung Yang, Jae Young Kim, Seong Jae Lee, Sung Sik Lee, and Ju Min Kim, Sheathless elasto-inertial particle focusing and continuous separation in a straight rectangular microchannel, Lab Chip **11**, 266 (2011).

[100] Jonas Hansson, J. Mikael Karlsson, Tommy Haraldsson, Hjalmar Brismar, W. van der Wijngaart, and Aman Russom, Inertial microfluidics in parallel channels for high-throughput applications, Lab Chip **12**, 4644 (2012).

[101] Liang-Liang Fan, Xu-Kun He, Yu Han, Jiang Zhe, and Liang Zhao, Continuous 3D particle focusing in a microchannel with curved and symmetric sharp corner structures, J. Micromech. Microeng. **25**, 035020 (2015).

[102] Dino Di Carlo, Jon F. Edd, Daniel Irimia, Ronald G. Tompkins, and Mehmet Toner, Equilibrium separation and filtration of particles using differential inertial focusing, Anal. Chem. **80**, 2204 (2008).

[103] T. Nizkaya, J. R. Angilella, and M. A. Bus, Inertial focusing of small particles in wavy channels: Asymptotic analysis at weak particle inertia, Phys. D: Nonlinear Phenom. **268**, 91 (2014).

[104] John Oakey, Robert W. Applegate, Erik Arellano, Dino Di Carlo, Steven W. Graves, and Mehmet Toner, Particle focusing in staged inertial microfluidic devices for flow cytometry, Anal. Chem. **82**, 3862 (2010).

[105] Shih-Kang Fan and Fu-Min Wang, Multiphase optofluidics on an electro-microfluidic platform powered by electrowetting and dielectrophoresis, Lab Chip **14**, 2728 (2014).

[106] Jae-Sung Park, Suk-Heung Song, and Hyo-Il Jung, Continuous focusing of microparticles using inertial lift force and vorticity via multi-orifice microfluidic channels, Lab Chip **9**, 939 (2009).

[107] Aram J. Chung, Dianne Pulido, Justin C. Oka, Hamed Amini, Mahdokht Masaeli, and Dino Di Carlo, Microstructure-induced helical vortices allow single-stream and long-term inertial focusing, Lab Chip **13**, 2942 (2013).

[108] Majid Ebrahimi Warkiani, Andy Kah Ping Tay, Bee Luan Khoo, Xu Xiaofeng, Jongyoon Han, and Chwee Teck Lim, Malaria detection using inertial microfluidics, Lab Chip **15**, 1101 (2015).

[109] Jun Zhang, Sheng Yan, Weihua Li, Gursel Alici, and Nam-Trung Nguyen, High throughput extraction of plasma using a secondary flow-aided inertial microfluidic device, RSC Adv. **4**, 33149 (2014).

[110] Ata Tuna Ciftlik, Maxime Ettori, and Martin A. M. Gijs, High throughput-per-footprint inertial focusing, Small **9**, 2764 (2013).

[111] Harm A. Nieuwstadt, Robinson Seda, David S. Li, J. Brian Fowlkes, and Joseph L. Bull, Microfluidic particle sorting utilizing inertial lift force, Biomed. Microdevices **13**, 97 (2011).

[112] Aram J. Chung, Daniel R. Gossett, and Dino Di Carlo, Three dimensional, sheathless, and high-throughput microparticle inertial focusing through geometry-induced secondary flows, Small **9**, 685 (2013).

[113] Bjorn Hammarstrom, Thomas Laurell, and Johan Nilsson, Seed particle-enabled acoustic trapping of bacteria and nanoparticles in continuous flow systems, Lab Chip **12**, 4296 (2012).

[114] L. Johansson, J. Enlund, S. Johansson, I. Katardjiev, M. Wiklund, and V. Yantchev, Surface acoustic wave-induced precise particle manipulation in a trapezoidal glass microfluidic channel, J. Micromech. Microeng. **22**, 025018 (2012).

[115] D.-C Seo, A. K. M. A. H. Siddique, B. Ahn, C. Kim, and S. Cho, Ultrasonic flow-through filtration of microparticles in a microfluidic channel using frequency sweep technique, J. Mech. Sci. Technol. **27**, 825 (2013).

[116] Jeremy J. Hawkes, Robert W. Barber, David R. Emerson, and W. Terence Coakley, Continuous cell washing and mixing driven by an ultrasound standing wave within a microfluidic channel, Lab Chip **4**, 446 (2004).

[117] Jonathan D. Adams, Christian L. Ebbesen, Rune Barnkob, Allen H. J. Yang, H. Tom Soh, and Henrik Bruus, High-throughput, temperature-controlled microchannel acoustophoresis device made with rapid prototyping, J. Micromech. Microeng. **22**, 075017 (2012).

[118] Jinjie Shi, Hua Huang, Zak Stratton, Yiping Huang, and Tony Jun Huang, Continuous particle separation in a microfluidic channel via standing surface acoustic waves (SSAW), Lab Chip **9**, 3354 (2009).

[119] Dario Carugo, Tobias Octon, Walid Messaoudi, Adam L. Fisher, Michele Carboni, Nick R. Harris, Martyn Hill, and Peter Glynne-Jones, A thin-reflector microfluidic resonator for continuous-flow concentration of microorganisms: A new approach to water quality analysis using acoustofluidics, Lab Chip **14**, 3830 (2014).

[120] Ola Jakobsson, Maria Antfolk, and Thomas Laurell, Continuous flow two-dimensional acoustic orientation of non-spherical cells, Anal. Chem. **86**, 6111 (2014).

[121] D. A. Johnson and D. L. Feke, Methodology for fractionating suspended particles using ultrasonic standing wave and divided flow fields, Sep. Technol. **5**, 251 (1995).

[122] A. Nilsson, F. Petersson, H. Jonsson, and T. Laurell, Acoustic control of suspended particles in micro fluidic chips, Lab Chip **4**, 131 (2004).

[123] A. Mueller, A. Lever, T. V. Nguyen, J. Comolli, and J. Fiering, Continuous acoustic separation in a thermoplastic microchannel, J. Micromech. Microeng. **23**, 125006 (2013).

[124] Jonathan D. Adams and H. Tom Soh, Tunable acoustophoretic band-pass particle sorter, Appl. Phys. Lett. **97**, 064103 (2010).

[125] Jeonghun Nam, Hyunjung Lim, Choong Kim, Ji Yoon Kang, and Sehyun Shin, Density-dependent separation of encapsulated cells in a microfluidic channel by using a standing surface acoustic wave, Biomicrofluidics **6**, 024120 (2012).

[126] Jinjie Shi, Shahrzad Yazdi, Sz-Chin Steven Lin, Xiaoyun Ding, I-Kao Chiang, Kendra Sharp, and Tony Jun Huang, Three-dimensional continuous particle focusing in a

microfluidic channel via standing surface acoustic waves (SSAW), Lab Chip **11**, 2319 (2011).

[127] Foram R. Madiyar, Lateef U. Syed, Christopher T. Culbertson, and Jun Li, Manipulation of bacteriophages with dielectrophoresis on carbon nanofiber nanoelectrode arrays, Electrophoresis **34**, 1123 (2013).

[128] Wei Cheng, Si-Zhe Li, Qian Zeng, Xiao-Lei Yu, Yu Wang, Helen Lai Wah Chan, Wei Liu, Shi-Shang Guo, and Xing-Zhong Zhao, Rapid microparticle patterning by enhanced dielectrophoresis effect on a double-layer electrode substrate, Electrophoresis **32**, 3371 (2011).

[129] Cheng-Hsin Chuang and Yao-Wei Huang, Multistep manipulations of poly(methyl-methacrylate) submicron particles using dielectrophoresis, Electrophoresis **34**, 3111 (2013).

[130] Nurul Amziah Md. Yunus, Hossein Nili, and Nicolas G. Green, Continuous separation of colloidal particles using dielectrophoresis, Electrophoresis **34**, 969 (2013).

[131] SiangHooi Ling, YeeCheong Lam, and ChinHock Kua, Particle streaming and separation using dielectrophoresis through discrete periodic microelectrode array, Microfluid. Nanofluidics **11**, 579 (2011).

[132] D. F. Chen, H. Du, H. Q. Gong, and W. H. Li, A 3-D microelectrode system for dielectrophoretic manipulation of microparticles, J. Phys.: Conf. Ser. **34**, 1008 (2006).

[133] Charles L. Asbury, Alan H. Diercks, and Ger van den Engh, Trapping of DNA by dielectrophoresis, Electrophoresis **23**, 2658 (2002).

[134] Cheng-Ping Luo, Andreas Heeren, Wolfgang Henschel, Monika Fleischer, and Dieter P. Kern, Contactless capturing of particles in liquid using pulsed alternating dielectrophoresis, J. Vac. Sci. Technol. B **24**, 3184 (2006).

[135] Chaohui Wang, Xiaozhang Wang, and Zhuangde Jiang, Dielectrophoretic driving of blood cells in a microchannel, Biotechnol. Biotechnol. Equip. **25**, 2405 (2011).

[136] Ming Li, Shunbo Li, Wenbin Cao, Weihua Li, Weijia Wen, and Gursel Alici, Improved concentration and separation of particles in a 3D dielectrophoretic chip integrating focusing, aligning and trapping, Microfluid. Nanofluidics **14**, 527 (2013).

[137] Nuttawut Lewpiriyawong, Kumaravel Kandaswamy, Chun Yang, Volodymyr Ivanov, and Roman Stocker, Microfluidic characterization and continuous separation of cells and particles using conducting poly(dimethyl siloxane) electrode induced alternating current-dielectrophoresis, Anal. Chem. **83**, 9579 (2011).

[138] Nuttawut Lewpiriyawong, Chun Yang, and Yee Cheong Lam, Continuous sorting and separation of microparticles by size using AC dielectrophoresis in a PDMS microfluidic device with 3-D conducting PDMS composite electrodes, Electrophoresis **31**, 2622 (2010).

[139] I-Fang Cheng, Cheng-Che Chung, and Hsien-Chang Chang, High-throughput electrokinetic bioparticle focusing based on a travelling-wave dielectrophoretic field, Microfluid. Nanofluidics **10**, 649 (2011).

[140] U. Lei, C. W. Huang, James Chen, C. Y. Yang, Y. J. Lo, Andrew Wo, C. F. Chen, and T. W. Fung, A travelling wave dielectrophoretic pump for blood delivery, Lab Chip **9**, 1349 (2009).

[141] I-Fang Cheng, Victoria E. Froude, Yingxi Zhu, Hsueh-Chia Chang, and Hsien-Chang Chang, A continuous high-throughput bioparticle sorter based on 3D traveling-wave dielectrophoresis, Lab Chip **9**, 3193 (2009).

[142] James T. Y. Lin, John T. W. Yeow, and Weijie Wan, Controlling two-dimensional movement of microparticles over an electrode array surface, Biomed. Microdevices **11**, 193 (2009).